AGU ADVANCING EARTH AND SPACE SCIENCE

Water Resources Research

RESEARCH ARTICLE
10.1029/2020WR027071

Key Points:
- Forest gap shape and edginess help determine the locations of postdisturbance changes in snow
- Changes in canopy density is not a good predictor of snowpack response to canopy disturbance at a fine scale
- Increases in seasonal temperature and higher insolation heighten postdisturbance changes in snow variability

Supporting Information:
- Supporting Information S1
- Movie S1

Correspondence to:
C. D. Moeser,
cmoeser@usgs.gov

Citation:
Moeser, C. D., Broxton, P. D., Harpold, A., & Robertson, A. (2020). Estimating the effects of forest structure changes from wildfire on snow water resources under varying meteorological conditions. *Water Resources Research*, *56*, e2020WR027071. https://doi.org/10.1029/2020WR027071

Received 8 JAN 2020
Accepted 20 OCT 2020
Accepted article online 29 OCT 2020

Estimating the Effects of Forest Structure Changes From Wildfire on Snow Water Resources Under Varying Meteorological Conditions

C. David Moeser[1], Patrick D. Broxton[2], Adrian Harpold[3], and Andrew Robertson[1]

[1]New Mexico Water Science Center, U.S. Geological Survey, Albuquerque, NM, USA, [2]School of Natural Resources and the Environment, University of Arizona, Tucson, AZ, USA, [3]Department of Natural Resources and Environmental Science, University of Nevada, Reno, Reno, NV, USA

Abstract Modeling forest change effects on snow is critical to resource management. However, many models either do not appropriately model canopy structure or cannot represent fine-scale changes in structure following a disturbance. We applied a 1 m^2 resolution energy budget snowpack model at a forested site in New Mexico, USA, affected by a wildfire, using input data from lidar to represent prefire and postfire canopy conditions. Both scenarios were forced with 37 years of equivalent meteorology to simulate the effect of fire-mediated canopy change on snowpack under varying meteorology. Postfire, the simulated snow distribution was substantially altered, and despite an overall increase in snow, 32% of the field area displayed significant decreases, resulting in higher snowpack variability. The spatial differences in snow were correlated with the change in several direction-based forest structure metrics (aspect-based canopy edginess and gap area). Locations with decreases in snow following the fire were on southern aspects that transitioned to south facing canopy edges, canopy gaps that increased in size to the south, or where large trees were removed. Locations with largest increases in snow occurred where all canopy was removed. Changes in canopy density metrics, typically used in snow models to represent the forest, did not fully explain the effects of fire on snow distribution. This explains why many models are not able to represent greater postfire variability in snow distribution and tend to predict only increases in snowpack following a canopy disturbance event despite observational studies showing both increases and decreases.

1. Introduction

Forests are key determinants of water supply, quality, and quantity, and their importance is increasing as freshwater resources become scarcer (Bates et al., 2008; Furniss et al., 2010). In the western United States, approximately 65% of the water supply comes from forested regions, and the majority of snowmelt originates from mountain forests (Furniss et al., 2010). Uncertainty in the fate of water originating from mountain forests is increasing due to climate change, variable land management strategies, and a variety of disturbances to vegetation, such as wildfire and bark beetles. These forest disturbances change biophysical processes (e.g., interception and transpiration) and are important drivers of hydrological variation (Buma & Livneh, 2017; Giles-Hansen et al., 2019; Wei et al., 2013; Zhang et al., 2017). Already, forest disturbance has affected many areas with seasonal snow. For example, more than 85% of the coniferous forests of the headwaters of the Rio Grande have been affected by the bark beetle (U.S. Forest Service, 2018, 2019). Furthermore, in the headwater regions of the Rio Grande and Colorado River Basins, burn areas are projected to increase 300% to 700% with a 1°C increase in mean global temperature (National Research Council (NRC), 2011). At the same time, we have a limited understanding of how these changes will affect downstream water resources (Sexstone et al., 2018).

Forest disturbance (e.g., from forest fires and bark beetle attacks) reduces canopy cover (density) and increases the prevalence of canopy gaps and edges (canopy structure heterogeneity), which, in turn, affect the spatial and temporal patterns of snow accumulation and ablation (Stevens, 2017). The reduction of forest cover decreases interception, which is a primary driver of heterogeneous snow accumulation patterns in forests (Figures 1a and 1b). This can result in increased snow accumulation on the ground because less snow is intercepted and subsequently sublimated. Sublimation of intercepted snow can be much higher than sublimation rates on the subcanopy snow surface (Essery & Pomeroy, 2001; Lundberg

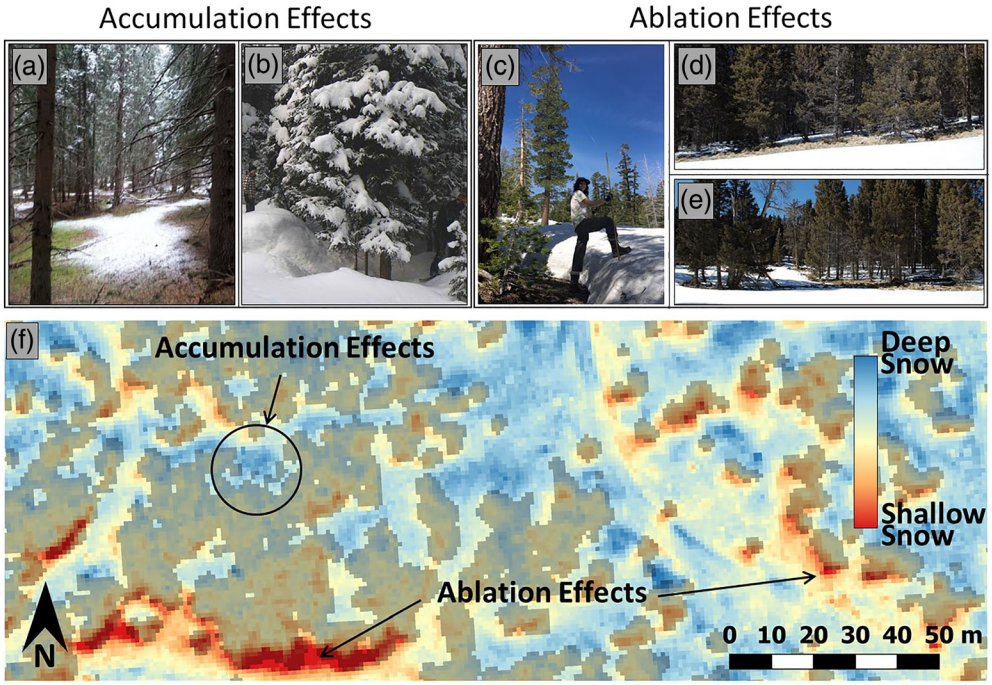

Figure 1. Accumulation and ablation processes: (a) Early season under-canopy accumulation modified by interception from the overhead forest structure. (b) Late season under-canopy snow accumulation affected by the interplay of interception, unloading, and sublimation, creating highly heterogeneous snow patterns; note individuals on the left and right of the tree for scale. (c–e) Ablation along south edges of forest gaps in high-radiation environments. (f) Lidar map showing snow depth differences between areas influenced by varying accumulation and ablation processes such as those depicted in (a)–(e) in a heterogeneous forest. Areas with canopy are shaded gray. Photo a: Giulia Mazzotti, Photo b: David Moeser, Photo c: Adrian Harpold, Photos d and e: Patrick Broxton.

& Halldin, 2001; Montesi et al., 2003; Suzuki et al., 2003), and in north central Colorado, USA, Sexstone et al. (2018) showed canopy sublimation was 4 times greater than subcanopy snow surface sublimation. At the same time, changes in canopy density and structure affect snow ablation (snowpack sublimation and melt) by changing the snow energy balance (Maxwell et al., 2019; Maxwell & St Clair, 2019; Sexstone et al., 2018). Reductions of canopy cover can increase shortwave radiation and decrease longwave radiation, not just underneath but also adjacent to forest stands. Net shortwave radiation also changes from increases in postdisturbance falling black carbon and burned woody debris that change the snow surface albedo (Gleason & Nolin, 2016; Gleason et al., 2013) and these changes have caused earlier snowmelt throughout the western United States, and have persisted for over a decade following a forest fire (Gleason & Nolin 2016).

Currently, there is a disagreement between modeling and observational studies in terms of whether forest disturbance increases or decreases snow water equivalent (SWE). Most current land surface models are not able to accurately represent horizontal canopy influences from shading, for example, to represent tree shadows or longwave radiation enhancement in canopy gaps. Observational studies have shown that there can be both increases and decreases in SWE after canopy changes (Biederman et al., 2015; Harpold, Biederman, et al., 2014; Stevens, 2017; Varhola, Coops, Bater, et al., 2010). Goeking and Tarboton (2020) synthesized 42 published studies that quantified the effects of canopy disturbance and changing canopy structure on snow water resources, and approximately half of the studies that were based directly on field observations displayed both increases and decreases in postdisturbance SWE. In contrast, to date, there has been just one modeling study (of 10 published modeling studies) that has simulated both increases and decreases in snow accumulation from changes in forest structure. This study, by Sun et al. (2018) integrated shading in canopy gaps in the Distributed Hydrology Soil Vegetation Model and simulated that a changing gap size can affect SWE estimates. However, specific canopy structure elements could not be analyzed due to the coarse nature of the model grid.

Canopy density and height estimates (e.g., leaf area index [LAI] and canopy closure [CC]) are typically the only metrics used in snow melt models to describe the canopy (Essery et al., 2009, 2013; Varhola & Coops, 2013). Unless these metrics are explicitly represented, or if further canopy structure parameters are integrated, the model is not able to simulate how snowpack is affected by the surrounding forest (Mazzotti et al., 2019; Mazzotti, Essery, Moeser, et al., 2020; Moeser et al., 2016). Horizontal position relative to the surrounding forest canopy and solar zenith angle are key determinants of the interactions between potential gains and losses in subcanopy snowpack following a canopy disturbance (Sun et al., 2018). Forest edges, for example, can display both the maxima and minima of net radiation (long and shortwave) and the relative amounts of snow water over a range of just a few meters (Golding & Swanson, 1986; Lawler & Link, 2011; Musselman et al., 2015; Pomeroy et al., 2009; Veatch et al., 2009) (Figures 1c–1e). Similarly, canopy gaps can display highly disparate snow patterns, depending upon the canopy gap size relative to the surrounding local tree height (Lawler & Link, 2011; Musselman et al., 2015). Until recently, most physically based representations of mass and energy fluxes have been developed for large spatial scales and ignore subgrid variability that occurs at the scale of individual trees. These large-scale representations can give markedly different results than those that include fine-scale representation of forest canopy. For example, Broxton et al. (2015) demonstrated that changing the resolution of a snow model from 1 m (where fine-scale canopy elements were resolved) to 100 m (where they were not) caused snow accumulation to decline by 25% and shortwave radiation to increase by 21% in some areas, despite using identical model physics.

New hyperresolution observations and enhanced computational resources are enabling snowpack models to be applied at the resolution needed to resolve tree-scale processes (e.g., 1 m). Light detection and ranging (lidar) observations are dramatically improving the spatial characterization of both forests and snowpacks (Deems et al., 2013; Harder et al., 2019; Harpold, Biederman, et al., 2014; Kostadinov et al., 2019; Mazzotti et al., 2019). Hyperresolution process modeling offers the potential to leverage lidar observations to predict the effects of fine-scale forest structure on snow water and energy budgets in ways not previously possible (Harpold et al., 2015). For example, hyperresolution models using lidar have been developed to model snow interception effects (Moeser, Stähli, et al., 2015; Moeser et al., 2016), as well as the transfer of radiative energy through the forest canopy at the scale of individual trees (Moeser et al., 2014; Musselman et al., 2013; Zellweger et al., 2019). To date, only a few tools are available that include lidar data to make high-resolution (1 m) spatially distributed predictions of the snowpack energy and mass budgets: the FSM2 (Mazzotti, Essery, Webster, et al., 2020) and SnowPALM (Broxton et al., 2015) models. These models capture snow depth (SD) variability in forests because they simulate a variety of two- and three-dimensional influences (e.g., canopy interception, shading of shortwave radiation, and longwave radiation). The capacity of these models to integrate high-resolution data allows them to avoid the oversimplification created by averaging canopy and terrain characteristics over large grid cell sizes and permits a more realistic analysis of fine-scale snow heterogeneity than is possible in coarser models.

This study uses the SnowPALM model and lidar data uniquely available for both prefire and postfire conditions to quantify the effects of canopy structure change from a high-severity fire (Jemez Mountains, New Mexico, USA) on subcanopy snow water resources. The study focuses on areas that display postfire reductions in snow water to answer the following research questions:

1. Research question one (RQ 1): Can the forest be partitioned into basic canopy structure classes (canopy gaps, canopy edges, and interior forest) to estimate postdisturbance changes in peak SWE (the maximum SWE value for the water year) and melt-out date (day when all snow is melted) more accurately than utilizing canopy density metrics?
2. Research question two (RQ 2): Can meteorological conditions (precipitation, temperature, and radiation) be used to estimate the magnitude of postdisturbance changes in peak SWE and melt-out date over time?

This work estimates the effects of canopy structure change initiated from a forest fire. It does not integrate the potentially large effects of changing snow surface albedo from black carbon and burned woody debris that is common after a wildfire (Gleason et al., 2019). However, determining relations between fine-scale canopy structure change and snow processes is an important step toward quantifying the potential long-term effects of landscape-scale forest change on water resources and can further highlight canopy structure metrics important for the representation of canopy disturbance in snow models. This is especially

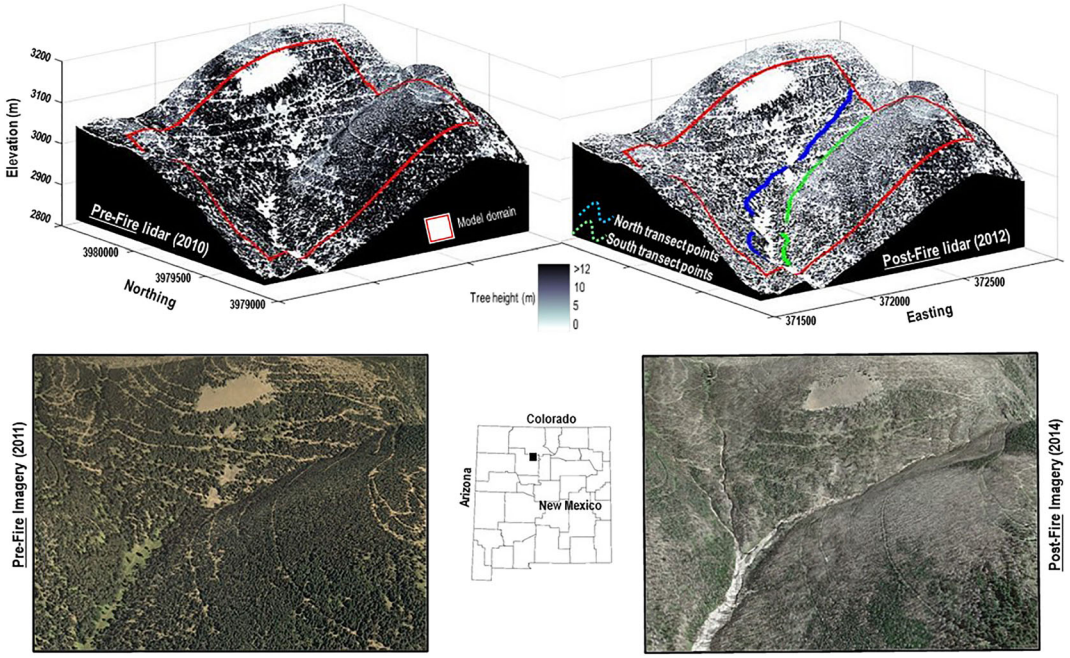

Figure 2. The upper left and right tiles display prefire and postfire lidar data for the model domain, where darker colors represent taller canopy elements. The 1.0 km north × 1.1 km model domain boundary is in red. Snow depth measurement transects are seen as blue and green lines in the upper left tile. The lower left and right tiles display prefire and postfire imagery for the model domain. The lower middle tile displays the generalized field location.

relevant for the Rio Grande Basin, in which the study area is located, because water is overallocated, much of this water originates as snow, and extreme forest changes are predicted for the future (Booker et al., 2005; deBuys, 2001).

2. Methods

2.1. Field Area

The study area (Figure 2) is located within the 2011 Las Conchas Fire burn perimeter in the Jemez River Basin within the Rio Grande Basin in northern New Mexico, USA. The site is located at the southern margin of the Rocky Mountains ecoregion, and the climate is semiarid with a mean annual precipitation of ~605 mm, about half of which occurs as snowfall. The mean annual temperature is 4.7°C, and the monthly mean temperature ranges from −5.2°C in January to 15.3°C in July (over a 30 year period to date; National Park Service, 2019). The 1.0 km north × 1.1 km east field area (Figure 2) was selected because it displayed a nonhomogenous canopy density and nonuniform canopy structures both prefire and postfire. Over 90% of the field area was classified as a high-severity fire (https://www.mtbs.gov/viewer/index.html). The area has a uniform elevation gradient and even distribution of north and south aspects and slope gradients. The southwest corner of the field area is located at 3979325 north and 371710 east (UTM Zone 13N NAD83) and has a mean elevation of 3,007 m and range of 2,813 to 3,182 m. Prior to the fire, the forest consisted primarily of mixed conifer species, including Douglas fir (*Pseudotsuga menziesii*), white fir (*Abies concolor*), blue spruce (*Picea pungens*), limber pine (*Pinus flexilis*), and ponderosa pine (*Pinus ponderosa*) along with scattered aspen (*Populus tremuloides*) and very little understory (Muldavin & Tonne, 2003).

2.2. Experimental Design

We created two models using a precalibrated version of the SnowPALM model for a 1.1 km^2 domain (1.1 million model pixels) in the Jemez Mountains to represent prefire and postfire canopy conditions. Thirty-seven years of equivalent meteorological forcing data were applied to both models (details of these simulations, as well as the model validation, are given is sections 2.3 and 2.4 below). Prefire lidar data were used to represent static forest canopy conditions ~1 year prefire, and the postfire lidar data were used to represent static forest

canopy conditions ~1 year postfire. Model differences were computed between the prefire and postfire simulations and then related to three generalized canopy structure classes on southern and northern terrain aspects: forest gaps, forest edges, and interior forest (areas that are not a forest gap or edge). The magnitude of change in peak SWE and melt-out date for the entire domain was then estimated from changes in precipitation, temperature, and radiation. Finally, canopy structure characteristics computed from the lidar data were also intercompared. This was done to highlight the efficacy of some potential model parameters compared to others to effectively represent changes in the forest.

Canopy density and forest structure metrics were derived from aerial lidar data. In June 2010, there was a lidar flyover of the Valles Caldera covering a total area of 722 km^2, including part of the Las Conchas Fire footprint (prefire lidar) with a mean point cloud density of 11.97 pts/m^2 (last returns: 9.27 pts/m^2) for the field area (https://doi.org/10.5069/G9319SVB). In May 2012, there was another lidar flyover over the area affected by the Las Conchas Fire (postfire lidar) covering a total area of 206 km^2 with a mean point cloud density of 17.99 pts/m^2 (last returns: 13.26 pts/m^2) (https://doi.org/10.5069/G9RB72JV). The postfire lidar point cloud density was reduced from a random point cloud reduction to better match the overall point cloud density and point spacing of the prefire lidar with a mean point cloud density of 12.05 pts/m^2 (last returns: 8.89 pts/m^2). The random point cloud reduction method was verified in an area approximately 4 km away from the field domain that was not burned. A comparison between canopy density metrics obtained by the prefire and postfire data sets in the unburned areas revealed negligible differences (see section 2.5.2).

2.3. Model Description and Updates

SnowPALM (Broxton et al., 2015) is a high temporal (1 h) and spatial (1 m) resolution mass and energy balance snowpack model that explicitly resolves the canopy structure at 1 m resolution to capture three-dimensional influences that trees and other topographic features have on the snowpack. The ability of SnowPALM to make spatially explicit predictions of shortwave radiation, longwave radiation, and wind distribution of snowfall based on three-dimensional canopy and terrain data makes SnowPALM ideal for simulating snow distributions in heterogeneous forests, and distinguishes it from many land surface models that use a binary classification of either open or under canopy. SnowPALM uses existing process formulations to account for topographic and vegetation influences on radiation (Mahat & Tarboton, 2012), interception (Liston & Elder, 2006; Pomeroy et al., 1998), wind distribution of snowfall (Winstral & Marks, 2002), and the turbulent exchanges of mass and energy at the snow surface. Radiative and turbulent exchange with the atmosphere is computed using a thin ($\leq$1 cm thick) surface layer. SnowPALM estimates pixels that are shadowed by comparing hourly zenith Sun angles to horizon angles due to varying canopy height in the direction of the Sun. Beers law is then used in the same manner as Mahat and Tarboton (2012) to compute attenuation of shortwave radiation through the canopy and is applied in model pixels that are shadowed from the canopy that are both beneath and behind canopy elements. Incoming longwave radiation is calculated based on an individual pixel's sky view factor, the temperature of nearby canopy and a calibrated horizontal distance as in Skartveit and Olseth (1987). Wind distribution of snowfall is calculated similarly to Winstral and Marks (2002), but also includes canopy height to estimate the wind fields. It is important to note that, in its current form, SnowPALM does not integrate temporal changes in snow albedo from postdisturbance increases of either black carbon, ash, or woody debris that can change the radiation distribution (Gleason et al., 2013, 2019; Gleason & Nolin, 2016).

This study benefits from the calibrated and validated model from Broxton et al. (2015) because that model was developed approximately 12 km away from this field area. However, two adjustments were made to better represent changes in canopy density and interception. First, this study uses an improved method to calculate LAI (see section 2.5.2), rather than scaling LAI from canopy cover fraction. Both of these metrics are an estimate of canopy density; however, LAI does not have a linear relation to canopy cover (Moeser et al., 2014). In addition, the interception parameterization, one of the main drivers of subcanopy snow heterogeneity, was changed from the Hedstrom and Pomeroy (1998) method, which was developed in the boreal forest, to the Moeser, Stähli, et al. (2015) model, which has been shown to perform better in lower latitude environments that display snow bridging on canopy elements. The Moeser, Stähli, et al. (2015) interception model requires, as input, CC and two additional canopy parameters that describe canopy openness: total gap area (TGA) and mean distance to canopy (MDC), which are also described in section 2.5. below. Due to

the inclusion of TGA and MDC, this model is able better represent interception in heterogenous canopy typical of the Jemez Mountains.

The prefire and postfire SnowPALM model was forced with the equivalent hourly precipitation, air temperature, wind speed, humidity, and downward shortwave and longwave radiation by downscaling gridded forcing data from the Parameter-Regression Independent Slopes Model (PRISM) adjusted Version 2 of the National Land Data Assimilation System (NLDAS-2, https://ldas.gsfc.nasa.gov/nldas/v2/forcing) from water year 1980 to 2017. The NLDAS-2 data are available on a 1/8° grid. In this study, a 1° grid of data centered around the field area was used to allow for enough data to utilize SnowPALM's built-in downscaling procedures. These procedures interpolate NLDAS data onto SnowPALM's 1 m grid by scaling hourly precipitation, temperature, humidity and pressure to elevation, and linearly interpolating other forcing variables (hourly wind speed/direction, downward shortwave/longwave radiation). For temperature and precipitation, local elevation-based relations are created for monthly PRISM maximum and minimum temperature means and precipitation sums, which are then compared to those computed from the NLDAS gridded data, resulting in monthly correction factors that are applied to every hour of forcing data (for temperature, the correction factor is weighted toward the maximum or minimum temperature correction factor based on time of day). Pressure and humidity are extrapolated using local (based on NLDAS data) pressure-temperature and humidity-temperature relations. Although there are differences between the NLDAS forcing data and those derived using field measured meteorological observations, there is a reasonably close correspondence at the Jemez site. The supplemental material of Broxton et al. (2015) shows a comparison between NLDAS variables including shortwave and longwave radiation and a variety of meteorological variables from field stations around the Jemez site.

2.4. Model Validation

The prefire and postfire scenarios used the same model parameters and forcing data downscaling methods as the model of Broxton et al. (2015), see Table 7 therein), who calibrated the model for a forested site approximately 12 km away and 30 m higher in elevation from this field area. A temporal validation was performed by comparing 10 years of SWE and SD measurements from a snow pillow (for SWE) and sonar (for SD) at the nearest SNOTEL site located in a forested area (Quemazon: https://wcc.sc.egov.usda.gov/nwcc/site?sitenum=708&state=nm) approximately 4 km to the southeast of our field site at an elevation of 2,896 m. These data were also parsed into accumulation, peak SWE, and ablation quantiles to validate model performance during the accumulation and ablation seasons. Melt-out dates and peak SWE dates were also analyzed. A similar comparison was made to 3 years of SWE measurements in a forested area, from a snow pillow managed by Sandia National Laboratory ([SNL]; Desilets, 2009) located 12 km southwest of the field area at an elevation of 3,095 m. All SnowPALM pixels that fell on top of a snow pillow were aggregated and compared to the snow pillow values.

A spatial validation was performed by comparing SnowPALM SD output to lidar-based SD estimates from a 1 km × 1 km domain located 11.5 km from the field domain at elevations ranging from 2,968 m to 3,098 m with a mean elevation of 3,022 m. The lidar based SD snapshot was created by Harpold, Guo, et al. (2014) by comparing a "snow-on" and a "snow-off" lidar flyover. The "snow-on" data were collected on 29 March 2010 (https://doi.org/10.5069/G9319SVB), and the "snow-off" data were collected during July 2010 (see above lidar description in section 2.2). These data were close to the mean peak SWE date for the field area. However, large portions of the domain displayed substantial midwinter ablation events common for this field area (Harpold, Biederman, et al., 2014). As in Broxton et al. (2015), the 1 m resolution SD snapshot was compared at four canopy-based subsets of the landscape within the validation domain: all pixels, under-canopy pixels (pixels that have canopy), near-canopy pixels (pixels that are located <15 m from a canopy element), and distant-canopy pixels (pixels that are >15 m from a canopy element) for all overlapping 1 m pixels. Broxton et al. (2015) further evaluated the model latent heat fluxes by a comparison to an Eddy Flux tower 12 km away, and can be seen in the supplementary information of that paper.

Finally, a SD measurement campaign in the burned area during ablation in March 2018 was performed. A total of 175 SD measurements on a southern aspect and 78 SD measurements on a northern aspect were made and georeferenced to ±10 cm using survey-grade positions acquired by using the real-time kinematic (RTK) survey technique (Figure 2). The measurements on the southern aspect were primarily 0 with a mean

of 0.6 cm of SD. As such, only the SD measurements on the northern aspects were analyzed. These measurements were then compared to the postfire model output.

2.5. Canopy Parameters

Canopy metrics were computed from aerial lidar data for prefire and postfire conditions. These include two canopy height metrics, two canopy density metrics, and five canopy structure metrics.

2.5.1. Canopy Height

Bare earth elevations were calculated from the snow-off lidar data by National Center for Airborne Laser Mapping (NCALM) with Terrascan software (https://www.terrasolid.com/products/terrascanpage.php). Mean canopy height was calculated as the mean value of the lidar point cloud minus the bare earth model for each 1 m pixel. The variable "max local tree height" was calculated as the maximum value of the lidar point cloud in a 5 m radius minus the bare earth model for each 1 m pixel.

2.5.2. Canopy Density

CC and LAI values were calculated for both prefire and postfire conditions from the aerial lidar data. LAI and CC were explicitly estimated for each pixel from the conversion of the bird's-eye aerial lidar perspective into a ground viewpoint angular perspective (synthetic images) using the method of Moeser et al. (2014). In this method, the aerial lidar data are flipped to represent a ground perspective, and the point cloud is converted into a polar coordinate system to mimic a hemispherical image taken with a fisheye lens with an equiangular projection. To distinguish between near and far canopy elements, each lidar return is printed as a black point whose printed point size linearly decreases with distance (printed point size distribution), so that the black points can overlap as leaves would overlap in a real hemispherical photograph.

For calibration and validation of the printed point size distribution of the synthetic images for both lidar data sets, 20 real hemispherical photos approximately 4 km outside of the field area were taken in 2016 under primarily low light conditions in order to maintain a good sky-canopy contrast (using a Canon 600D with a Sigma 4.5 mm F2.8 EX DC HSM circular fisheye lens) in an area that was not burned but had lidar data from both flyovers. The locations of the photographs were taken under a range of canopy densities and georeferenced to $\pm$10 cm using survey-grade positions acquired by using the RTK survey technique. The final printed point size distribution for both data sets was optimized and set to 0.4 pixels for the farthest elements and 7.2 pixels for the nearest elements from a minimization of the root mean square error that compared LAI estimates from the synthetic images and hemispheric photos in ~3,000 different printed point size distribution scenarios. All lidar data below 1.25 m in height were removed to mimic the standard height of a hemispheric photo, and any data located outside a 150 m radius of each point were removed. The synthetic images and the hemispherical photos were analyzed with the image analysis software, Hemisfer, Version 2.2 (Schleppi et al., 2007; http://www.schleppi.ch/hemisfer/) to estimate CC and LAI at each pixel. The CC and LAI estimates from the synthetic images were then compared against CC and LAI values from the hemispheric photos. The prefire synthetic images displayed an RMSE of 0.048 and 0.31 for CC and LAI, respectively, and a correlation coefficient of 0.91 and 0.85 for CC and LAI, respectively. The postfire synthetic images displayed an RMSE of 0.052 and 0.32 for CC and LAI, respectively, and a correlation coefficient of 0.90 and 0.84 for CC and LAI, respectively. Within the model, LAI and CC were partitioned by canopy height, where any pixel that had a calculated canopy height value less than 1.25 m was then given a value of 0.

There are other available methods for transferring lidar to CC and LAI. However, this method allowed for ground truthing, and calibration, important not just to validate the density estimates but also to ensure that the differences between the prefire and postfire estimates were not because of different lidar data sources.

2.5.3. Canopy Structure Metrics

In addition to canopy height and density metrics, canopy structure metrics, or measures of the spatial arrangement of canopy elements, were calculated both as direct input into SnowPALM and to compare with model results. These included canopy openness metrics (MDC and TGA, which were used as inputs into SnowPALM; see section 2.3) and canopy edginess metrics (edginess to the north, edginess to the south, and nondirectional edginess; which were used to compare to model results). All canopy metrics were calculated for each 1 m grid cell using the prefire and postfire lidar data.

The metrics were computed using an updated version of the vector searching algorithm first introduced by Moeser, Morsdorf, et al. (2015). The algorithm first scans lidar data for the presence of canopy elements in 192 unique horizontal directions on the planar surface from searching vectors originating at the center of

each 1 m grid cell. For each vector, a distance between the center of the grid cell and the closest canopy feature, which is in the directional path of the vector (end point), is defined. All end points from the 192 vectors are connected and a two-dimensional polyshape is created. TGA is defined as the area of the two-dimensional polyshape. MDC is defined as the mean length of each of the 192 vectors.

The vector searching algorithm was further updated to estimate the canopy edge of a forest gap (edginess) metrics based on aspect (north and south) and canopy gap diameter relative to the surrounding canopy height. These metrics included (1) "edginess to the south," (2) "edginess to the north," and (3) "nondirectional edginess" (the sum of "edginess to the south" and "edginess to the north"). Existing metric output from the vector searching algorithm ("minimum distance to canopy to the north," "mean distance to canopy to the north," "minimum distance to canopy to the south," and "mean distance to canopy to the south") (see Moeser et al., 2015a, for precise metric definitions and methodology) were combined to derive an aspect based edginess parameter with a maximum value of 1 and a minimum value of 0 based upon a threshold value relative to the mean tree height for the area. If the pixel was in an opening ≥2 m from a canopy element on a gap edge, then a "NaN" value was assigned. A 3*H* (where *H* is the mean height of canopy in the model domain) diameter gap was chosen as a threshold for the edginess calculations. For example, if a pixel was located on a canopy edge with the canopy gap located to the south with a gap diameter of 1.5*H*, the grid cell would receive a value of 0.5 (1.5*H*/3*H*) for "edginess to the south" and 0 for "edginess to the north." Any values greater than the 3*H* threshold received a value of 1. The choice of "3*H*" was based on prior research that related snowpack and melt to the size of canopy gaps. Prior work has shown that canopy edginess becomes important as a predictor of "high- and low-energy" forested environments, where high- and low-energy environments are defined as areas with more or less net radiation than nonforested areas (Bernier & Swanson, 1993; Church, 1933; Golding & Swanson, 1986; Lawler & Link, 2011; Stegman, 1996). At a 47°N latitude field site, Lawler and Link (2011) found canopy gaps with diameters >3*H* have high-energy conditions on their northern edges (south facing edge), while those that have diameters between 1*H* and 2*H* have low-energy conditions. High-energy and low-energy forested environments generally have lower or higher snow accumulation, respectively.

2.6. Model Output and Analysis

2.6.1. RQ1—Correlation of Forest Structure Classes to Locations of Postfire Changes in Snow

The prefire canopy metrics (prefire state) and change in the canopy metrics (postfire state − prefire state) were spatially plotted to visually define locations in the field area where changes in peak SWE (Δ peak SWE) and melt-out date (Δ melt-out date) occur. The prefire metrics and postfire change in metric values were then used in a secondary regression analysis to define potential correlations from the visible relations in the spatial plots. The regression equations may be further used to improve understanding of the potential predictive power of three basic canopy structure classes: canopy edges, canopy gaps, and the interior forest (areas that are not a forest gap or edge) at representing Δ peak SWE and Δ melt-out date. The domain was split into north and south aspects and the analysis was performed independently on each aspect. The specific equations are presented in the supporting information, and explanatory statistics from those equations are presented in section 3.4.

2.6.2. RQ2—Correlation of Meteorology to Site-Based Changes in Snow

The model output and basic meteorological variables from all model pixels were parsed into accumulation, ablation, and snow cover duration periods. The accumulation period was defined as the first day before peak SWE that was ≤0.01*peak SWE to peak SWE. The ablation period was defined as peak SWE to the first day after peak SWE that was ≤0.01*peak SWE. Snow cover duration was the range between the first day of accumulation and the last day of ablation.

Absolute changes (postfire − prefire) in (1) mean peak SWE over the field area, (2) peak SWE range for the field area, (3) mean melt-out date over the field area, and (4) melt-out date range for the field area were quantified for each water year. Ranges were calculated to represent variability and were defined as the difference between the 75th percentile and the 25th percentile value of the field area. Relations were developed between each of these four snow metrics and up to three meteorological parameters (precipitation, air temperature, and downward shortwave radiation during accumulation, ablation, and snow cover duration) from a regression analysis using data from all water years with cumulative precipitation greater than 100 mm.

Table 1
Statistics Comparing SnowPALM SWE and SD Estimates to the SNOTEL (Quemazon) SWE and SD Measurements Between Water Year (WY) 2004 to WY 2014 As Well As the SNL SWE Measurements Between WY 2008 to WY 2010 for the Entire Period), Peak Snowpack Period, Accumulation Period, Ablation Period, Peak SWE Date, and Melt-Out Date

	Quemazon SNOTEL (WY 2004–2014)						SNL (WY 2008–2010)			
	SWE/SD (mm)				Date (days)		SWE (mm)		Date (days)	
	Entire period	Peak snowpack period	Accumulation period	Ablation period	Peak snowpack	Melt-out	Entire period	Peak snowpack	Peak SWE	Melt-out[a]
R^2	0.93/0.84	0.93/0.87	0.91/0.64	0.94/0.94	0.54/0.93	0.76/0.36	0.9	0.99	0.51	[a]
Mean bias	−4.5/56.1	−12.4/140.6	0.2/51.2	−30.3/14.42	1.4/−4.8	−3.0/8.9	−8.6	−5.97	−12	−0.5[a]
% difference	−12.3/8.4	−8.8/14.1	−2.0/0.41	−6.6/11.4	1.0/−2.6	−1.7/−2.3	−10.5	0.52	7.27	0.14[a]

(*Note*. See Figure 3d schematic for more specific data cutoffs. Due to data gaps with the SNL snow pillow, statistics for accumulation and ablation periods are not available.)
[a]Denotes just two melt-out data points.

3. Results

3.1. Model Validation

The model was well correlated to both the Quemazon and SNL snow pillows during all phases of the snow season including peak SWE, accumulation, ablation, melt-out date, and peak SWE date with a coeffiecient of determination (R^2) ranging between 0.90 and 0.93 for all estimates between the start of accumulation and melt-out date (Table 1 and Figure 3). Peak SWE was estimated with a mean R^2 of 0.96, and had a negative mean bias of 9.2 mm (a 4.6% bias). Melt-out date had an R^2 of 0.76 and had a negative mean bias of 3 days for the Quemazon SNOTEL and positive ½ day bias at the SNL snow pillow, though only two melt-out dates were available at the SNL snow pillow due to data gaps. SWE during accumulation and ablation had R^2 values of 0.91 and 0.94, respectively, with a slight bias of 0.2 mm during accumulation and a negative bias of 30.3 mm (a 6.6% mean bias) during ablation (Table 1 and Figure 3). SD displayed slightly reduced performance as compared to the SWE validation statistics and instead of a small negative bias, SD displayed a positive 8.4% mean bias and an R^2 of 0.84 for all data between start of accumulation and melt-out date. Although most SWE variability is reflected in SD variability, a reliance upon SD measurements also integrates errors with snow density estimates.

SnowPALM SD estimates displayed similar fine-scale trends as the lidar derived SD estimates (29 March 2010) (Figure 3). Spatially, the mean R^2 was 0.33 with a mean positive bias of 49 mm (a 5.7% mean bias). SnowPALM had higher SD in under-canopy and near-canopy pixels (positive mean bias of 62 and 43 mm, respectively) and lower SD in open pixels as compared to the lidar snapshot. Both data sets showed a large SD variability. Most of the variance was due to canopy shading where relatively shallow snow was seen on the south sides of canopy pixels relative to deeper snow on the north of canopy pixels (Figure 3 insets), which demonstrated an earlier start to the ablation season and increased midwinter ablation in these locations. Except for open pixels, where the coefficient of variation (CV) is 0.12 for both data sets, the SnowPALM SD estimates displayed slightly higher variation than the lidar SD snapshot. SnowPALM had a CV of 0.25 and 0.22 for under-canopy and near-canopy pixels, respectively, while the lidar snapshot had a CV of 0.21 and 0.18, respectively. The comparison of the postfire SnowPALM estimates to the field measurements in the burned plot showed similar results. These measurements had a mean measured SD of 25 cm and when compared to the model, had an R^2 of 0.68 and a mean bias of 1.7 cm or 6.8%.

3.2. Canopy Parameters

The postfire lidar data were collected 1 year and 11 months after the prefire lidar data and 11 months after the fire. This short time period means that the differences between the two lidar data sets were primarily caused by the forest fire, as most dead trees were still standing, and there was essentially no forest recovery/regrowth prior to the postfire lidar. As such, most model pixels show decreases in canopy density, increases in canopy openness (TGA, MDC), increases in edginess (edginess to the south, north, and nondirectional), and decreases in canopy height. However, some pixels that were not affected by the fire had limited canopy growth not related to recovery between these two time periods. Specifically, 1.5% of the model

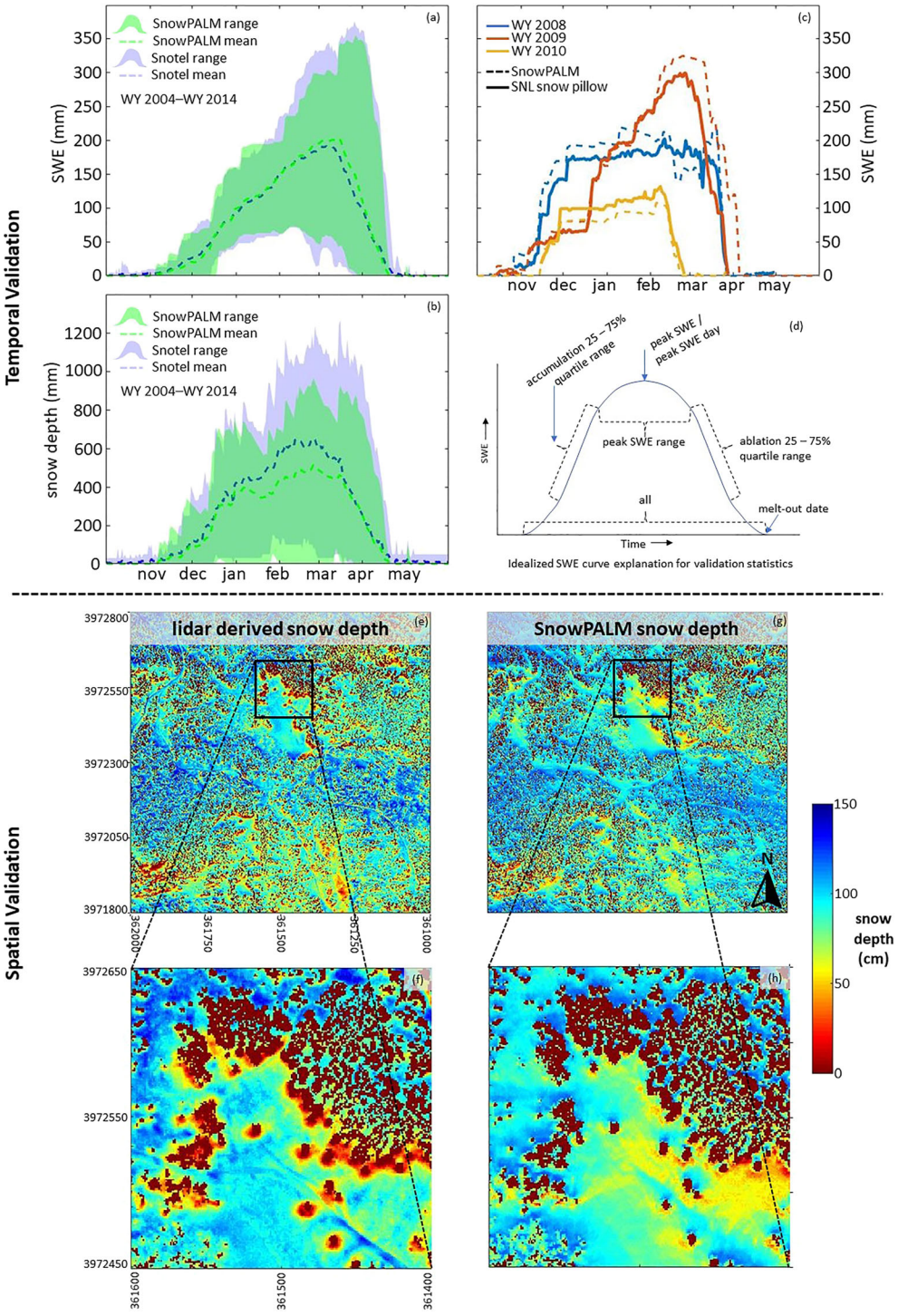

Figure 3. (a and b) Comparisons of SnowPALM to the Quemazon SNOTEL data. (c) A comparison of SnowPALM to the SNL SWE measurements. (d) Various aspects of a generalized SWE curve used in the validation statistics in Table 1. (e and f) Snow depth maps from the lidar snapshot for 29 March 2010. (g and h) Snow depth maps from SnowPALM for 29 March 2010.

pixels had increases in canopy density, 0.3% of the field area had decreases in canopy openness, 0.5% had decreases in canopy edginess, and 0.2% had increases in mean canopy height. Canopy density metrics (CC and LAI) had much lower percent differences between data sets (prefire vs. postfire lidar) as compared to

Table 2
Canopy Metric Values and Percent Differences From the Prefire and Postfire Lidar Data

Canopy metric		Prefire	Postfire	% Difference
Density	Canopy closure	**0.71** [0.15–0.95]	**0.62** [0.14–0.93]	**−12%** [−36–0]
	Leaf area index	**1.25** [0.1–3.35]	**0.89** [0.09–2.51]	**−26%** [−65–0]
Openness	Total gap area (m^2)	**639** [2–20,554]	**1839** [2–22,639]	**81%** [0–100]
	Mean distance to canopy (m)	**6.5** [0.9–79.1]	**16.9** [0.9–83.8]	**66%** [0–98]
Edginess	Edginess to the south	**0.05** [0–1]	**0.11** [0–1]	**41%** [0–100]
	Edginess to the north	**0.05** [0–1]	**0.11** [0–1]	**40%** [0–100]
	Nondirectional	**0.09** [0–1]	**0.20** [0–1]	**45%** [0–100]
Height	Mean height (m)	**4.96** [0–22.54]	**1.95** [0–15.20]	**−62%** [−100–0]
	Maximum height (m)	**17.08** [0–37.06]	**15.35** [0–34.23]	**−12%** [−100–0]

Note. Values = mean [min–max].
Mean values are in bold. The range of values from minimum to maximum are in brackets.

canopy openness and canopy edginess metrics. Mean percent difference of CC prefire to postfire was 12% with an absolute range of 0% to 36% (Table 2). For LAI, the absolute and mean percent difference approximately doubled. The canopy openness and edginess metrics had substantially higher mean percent differences prefire to postfire and displayed absolute percent changes ranging from 0% to 100% within the field area (Figure 4). Max tree height displayed low mean percentage difference values similar to CC (12%). However, unlike the density metrics, max tree height showed an absolute range of change values from 0% to 100%. These statistics would change with a varying postfire lidar flyover date, and values could be both larger and smaller depending on the timing of the lidar snapshot relative to the fire.

3.3. Simulation of Snowpack

There was a large interannual range of SWE values and melt-out dates in the field area. Peak SWE, for example, ranged from 5 to 455 mm for the prefire and postfire simulations. Similarly melt-out date ranged from years without any snow to melt and a maximum melt-out date of 21 May for the prefire and postfire simulations. The mean, median, and range of values for postfire peak SWE and melt-out date were higher and later for all years than for prefire simulations. Despite an overall increase in SWE after the fire, 32% of the field area displayed decreases in peak SWE and earlier melt-out dates relative to the prefire data. On southern

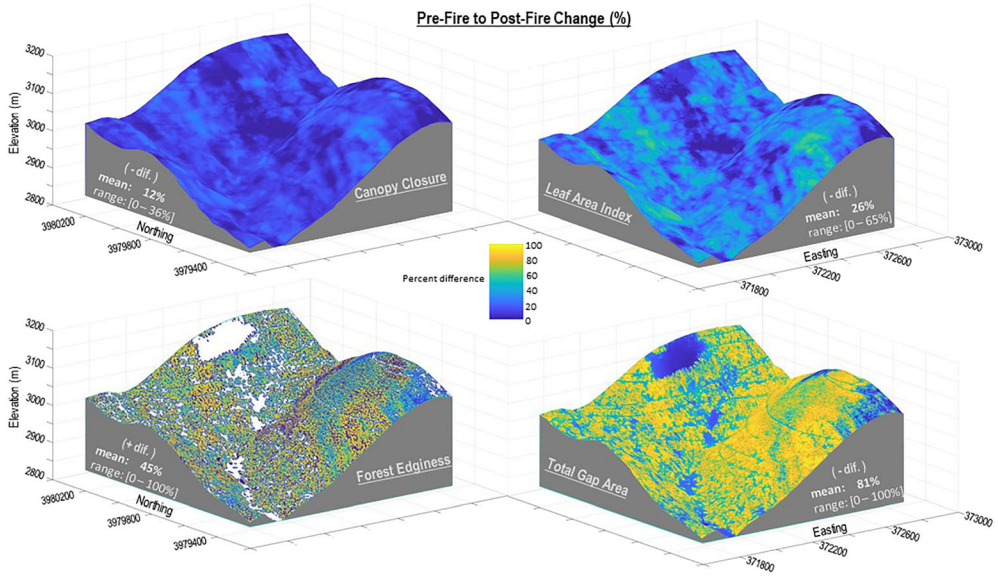

Figure 4. Changes in canopy density metrics (negative changes) on the upper row (CC on the left and LAI on the right) and canopy structure metrics (positive changes) on the lower row (nondirectional edginess on the left and total gap area on the right) at a 1 m scale.

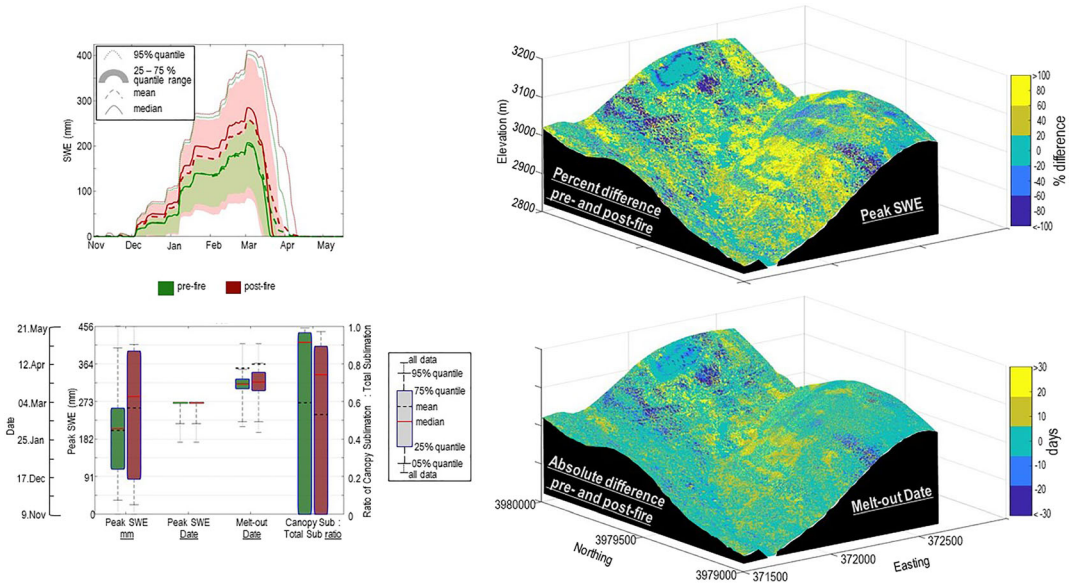

Figure 5. Model output overview for the Water Year 1992, which had the highest peak SWE. The upper left tile displays prefire (green) and postfire (red) SWE. The lower left tile displays the prefire (green) and postfire (red) range of peak SWE, peak SWE date, melt-out date, and canopy sublimation: Total sublimation for the model domain. The upper right tile displays the percent difference in peak SWE between the prefire and postfire models. The lower right tile displays the absolute difference in melt-out date between prefire and postfire models.

aspects, 36% and 39% of the field area displayed a reduction in peak SWE and earlier melt-out date, respectively. On northern aspects, 29% and 26% of the field area displayed a reduction in peak SWE and earlier melt-out date, respectively. Postfire increases and decreases (peak SWE and melt-out date) were always positioned in similar locations in the field area, and these locations could be defined from the generalized canopy structure classes.

Figure 5 displays model differences in melt-out date and peak SWE for water year 1992 that displayed the highest peak SWE value of all water years. For this water year, the 25–75% interquartile range (IQR) of prefire peak SWE values ranged from 109 and 257 mm, while the postfire values were between 84 and 395 mm. Similarly, the IQR of post fire melt-out dates were almost double those of the prefire scenario. The supporting information Movie S1 (wy_1992_SWE_through_time.mp4) displays the prefire and postfire model SWE estimates and the absolute difference between the two through time (for water year 1992) for all model pixels. The largest differences between the two models are during peak SWE. However, postfire differences (relative to the prefire model) are established during accumulation season from accumulation processes and stay consistent through ablation season. Note that Figure 5 shows an example for a single water year, but these findings are consistent for all modeled years.

3.4. RQ1—Correlation of Canopy Structure Classes to Locations of Postfire Changes in Snow

3.4.1. Canopy Edges

No visible spatial trends were seen with the nondirectional edginess metric to Δ peak SWE and Δ melt-out date. However, when canopy edginess was broken up into edginess to the north (Edge.N) and edginess to the south (Edge.S), locations of similar Δ melt-out date trends grouped together. Specifically, earlier postfire melt-out dates were visible when the canopy transitioned to a higher energy environment, or large south facing edges on southern aspects. Figure 6 shows that earlier postfire melt-out dates (in red) primarily appear as the size of the canopy edge approaches a maximum 3*H* edginess value. Specifically, this can be seen on the bottom left tile of this figure when the prefire edginess value (on the *y* axis) and postfire change in edginess value (on the *x* axis) approach the bold black line, which represents a maximum 3*H* edginess value.

These locations represent areas in the model domain that transitioned to higher energy south facing slopes with a canopy gap opening to the south. A disturbance increases the size of the canopy gap in front of an edge and consequently the canopy edginess value is increased. This allows for an increase in direct incoming solar

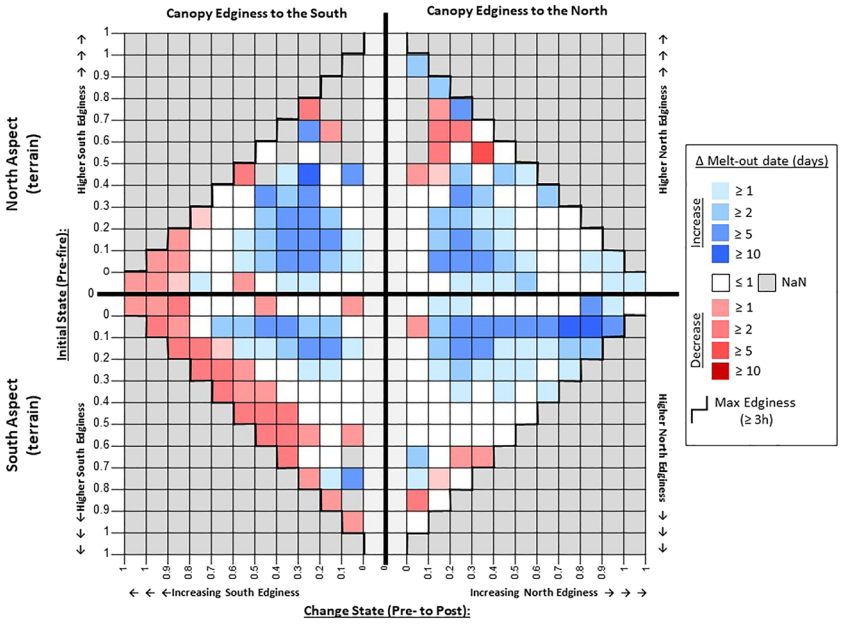

Figure 6. Modeled postfire changes in melt-out date as a function of postfire changes in canopy edginess on northern aspects (upper row) and southern aspects (lower row), south facing edges (left column) and north facing edges (right column). Δ melt-out date is binned according to the prefire edginess value represented on the *y* axis and the postfire change in edginess, on the *x* axis. The additive of the prefire state and change state cannot be greater than the maximum edginess value of 1 which represents an edge that sites on a 3*H* canopy gap, represented by the diagonal bold black line.

radiation and a decrease in canopy shading. However, the interplay of solar radiation and shading changes throughout the season. As the season progresses and the mean daily solar elevation angle increases, the amount of shading in these areas is reduced. This increases the potential solar radiation. As such, snow distributions in these areas are more ablation dominated than accumulation dominated, and melt-out date is more affected than peak SWE. There were also locations on northern aspects that displayed earlier postfire melt-out dates. However, larger changes in the canopy were necessary in these lower radiation environments to display earlier postfire melt-out dates. Neither Edge.S nor Edge.N displayed large areas with reductions in postfire peak SWE. Locations on canopy edges with reductions in Δ melt-out date were on average 2 days earlier with a maximum of 6 days earlier melt-out. Locations on canopy edges with reductions in Δ peak SWE showed a mean postfire reduction of 7 mm or 12% and a maximum of 55 mm or 77%.

Regressions were created using prefire Edge.S with the postfire change in Edge.S to determine how much Δ melt-out date and Δ peak SWE model variance the generalized canopy structure variables could estimate. Estimates of Δ peak SWE displayed R^2 values of 0.49 and 0.72 and a RMSE of 30.9 and 11.0 mm on north and south facing terrain aspects, respectively (Table 3; all p values were <0.01). Estimates of Δ melt-out date displayed R^2 values of 0.56 and 0.76 and a RMSE of 1.5 days and 1 day on north and south facing terrain aspects, respectively (Table 3; all p values were <0.01). No significant correlations were found without a log transform of the variables. This highlights a simulated nonlinear spatial distribution of snow from the middle of a gap to the edge of a gap during ablation.

Table 3
R^2 and Root-Mean-Square Error Values (RMSE) of Regressions for Each Canopy Structure Class That Estimate the Postfire Change in Peak SWE and Melt-Out Data on North and South Aspects

	Δ Peak SWE (mm)		Δ Melt-out date (days)	
	North aspect	South aspect	North aspect	South aspect
Canopy edges	0.49 (30.9)	0.72 (11.0)	0.56 (1.5)	0.76 (0.9)
Canopy gaps	0.70 (2.9)	0.30 (59)	0.35(1.5)	0.36 (5.5)
Interior forest	0.78 (29.9)	0.77 (35.0)	0.78 (2.0)	0.78 (2.0)

Note. RMSE values are in parentheses and have units of mm and days for peak SWE and melt-out date, respectively. All p values were less than 0.01.

3.4.2. Canopy Gaps

The TGA metric displayed no visible spatial trends to Δ peak SWE and Δ melt-out date. However, when the change in canopy gap shape was analyzed, visual patterns were seen in the groupings of Δ peak SWE and Δ melt-out date. Prefire TGA values were used with the postfire change in "distance to canopy edge" values ("distance to south edge of a gap,"

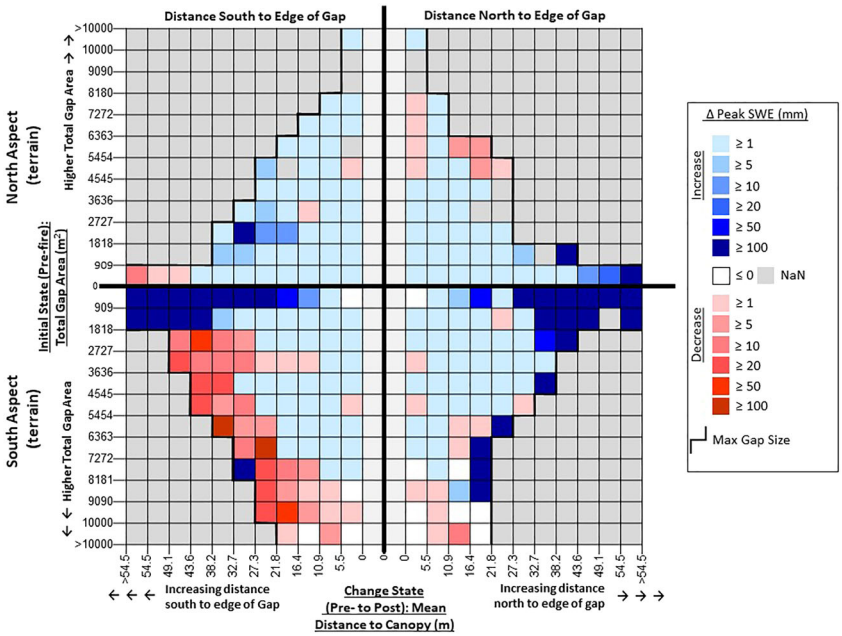

Figure 7. Overview of postfire changes in peak SWE as a function of postfire changes in gap area on northern aspects (upper row) and southern aspects (lower row), as gap size increases to the south (left column) and as gap size increases to the north (right column). Δ peak SWE is binned according to the prefire total gap area value, represented on the *y* axis and the postfire change in distance to canopy, on the *x* axis. The additive of the prefire state and change state cannot be greater than the gap area in the domain which is represented by the diagonal bold black line.

"distance to north edge of a gap") to define directional changes in gap size. As with canopy edges, changes in gap shape displayed earlier postfire melt-out date in areas that transitioned to high-energy environments, which in this case is defined as a model pixels position in a gap relative to a southern aspect. However, unlike canopy edges, when the gap shape transitioned to high-energy environments, peak SWE was also reduced. This is represented in Figure 7 from a visualization grid of binned model output data that represents prefire TGA values on the *y* axis and the change in "distance to canopy edge" values on the *x* axis. Specifically, when the sum of the prefire TGA value and the postfire change in "distance to south edge of a gap" on southern aspects reached a maximum gap area displayed as a bold black line in Figure 7, the largest decreases in Δ peak SWE were seen (bottom left tile of Figure 7). Within a gap, increasing the distance to the south edge of the gap, represents areas where the south edge of a gap has been removed by the fire. This increases the potential for direct incoming solar radiation and decreases the potential for canopy shading. There were fewer areas with postdisturbance reductions on northern aspects compared to southern aspects and only when the change in "distance to canopy edge" was close to the maximum amount of change, were any reductions seen in these areas.

Canopy gaps displayed larger areas with earlier postfire melt-out dates and peak SWE reductions as compared to canopy edges. Specifically, 28% of the field area that had increases in gap area to the south displayed reductions in peak SWE with a mean reduction of 23 mm SWE or 9% and a maximum reduction of 117 mm or 57%. This is more than triple the mean change in peak SWE as compared to the areas with increasing canopy edginess. Forty-five percent of the field area that had increases in gap area to the south displayed earlier melt-out dates with a mean decrease of approximately 4 days and a maximum decrease of 24 days.

Prefire TGA values in tandem with the postfire change in distance to the south edge of gap values were able to capture between 30% and 70% of the simulated Δ postfire peak SWE and melt-out date differences. Estimates of Δ peak SWE displayed R^2 values of 0.70 and 0.30 and a RMSE of 2.9 and 59 mm on north and south facing terrain aspects, respectively (Table 3; all p values were <0.01). Estimates of Δ melt-out date displayed R^2 values of 0.35 and 0.36 and a RMSE of 1.5 and 5.5 days on north and south facing terrain aspects, respectively (Table 3; all p values were <0.01). No significant correlations were found without a

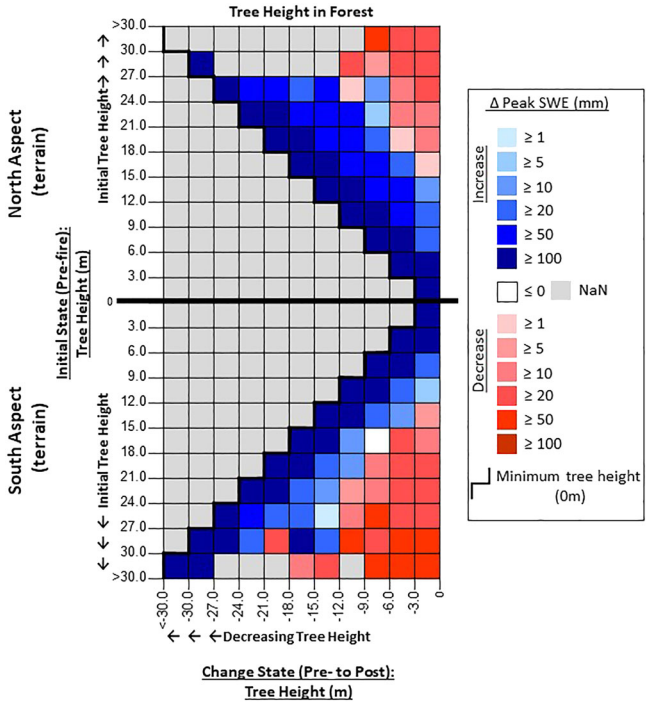

Figure 8. Overview of postfire changes in peak SWE as a function of postfire changes in tree height on northern aspects (upper row) and southern aspects (lower row) in the interior forest (domain that is not an edge or a gap). Δ peak SWE is binned according to the prefire tree height value, represented on the *y* axis and the postfire change in tree height, on the *x* axis. The additive of the prefire state and change state cannot be less than 0 or the minimum tree height, which is represented by the diagonal bold black line.

log transform of the variables. Like the canopy edge structure class, this highlights a simulated nonlinear spatial distribution of snow based upon relative position to the surrounding canopy.

3.4.3. Interior Forest

The interior forest, areas that are not a forest gap or edge, displayed no visible spatial trends to Δ peak SWE or Δ melt-out date when canopy density (CC and LAI) and sky view fraction metrics were used as predictors. Similarly, no spatial patterns were seen between mean canopy height and Δ peak SWE or Δ melt-out date. However, maximum local tree height (MTH) displayed a visible linear relationwith Δ peak SWE and Δ melt-out date. Figure 8 displays a visualization grid of prefire MTH and the postfire change in MTH. Significant increases in peak SWE and later melt-out date were found as the change in MTH decreased to a minimum demonstrated by the bold diagonal line in Figure 8. If the entire interior forest was removed or if large trees were removed and small trees were left, then there were large increases in peak SWE and later melt-out date. However, in some cases, if large trees were removed or the canopy height of large trees was reduced while the underlying canopy was left intact, then there were large decreases in peak SWE and earlier melt-out date. These decreases were most prevalent on southern exposed slopes. This analysis indicates that large trees played a more significant role than small trees, and that the effect of removing larger trees was more substantial than the effect of removing smaller trees.

Thirty percent of the interior forest displayed postfire peak SWE decreases, which had a mean of 31 mm or 17% with a maximum decrease of 84 mm or 58%. Thirty-one percent of the partitioned domain displayed an earlier melt-out date that was, on average, 2 days earlier and ranged to a maximum of 6 days earlier than the prefire states. This contrasts with edginess and gap areas, where the change in melt-out date was higher relative to the change in peak SWE. This highlights that accumulation processes are more important for modifying snow distributions in the interior forest, but ablation processes are more important in gaps and forest edges.

Prefire MTH values in tandem with the postfire MTH values were able to capture greater than 75% of the modeled Δ postfire peak SWE and melt-out date differences. Estimates of Δ peak SWE displayed R^2 values of 0.78 and 0.77 and a RMSE of 29.9 and 35.0 mm on north and south facing terrain aspects, respectively (Table 3; all p values were <0.01). Estimates of Δ melt-out date displayed an R^2 value of 0.78 and a RMSE of 2.0 days on both north and south facing terrain aspects (Table 3; all p values were <0.01).

3.5. RQ2—Correlation of Meteorology to Site-Based Changes in Snow

3.5.1. Peak SWE

Depending on the water year, postfire mean peak SWE values for the whole field area ranged from 5 mm on low snow years to 55 mm higher on high snow years than prefire values and represent a 9% to 92% postfire increase (mean increase of 35%). The variability, as demonstrated by the IQR, of postfire SWE values for the field area was significantly higher than prefire values. Postfire increases in IQR were between 20 and 130 mm for all water years and represent a 68% to 447% increase (mean increase of 144%). Increases in postfire peak SWE variability for the site always included areas that displayed both higher and lower postfire peak SWE values within the domain relative to the prefire model (see Figure 5).

Interannual variations in Δ mean peak SWE were best estimated with the (1) mean snowfall ($\overline{snow}$) and (2) the mean temperature ($\overline{ta}$) during the snow cover duration period (scd) (Equation 1). This relation resolved 66% of the data variation; mean snowfall accounted for 59% and temperature accounted for the remaining 7%, with an RMSE of 6.12 mm and a p value <0.01. Predictions of Δ peak SWE IQR (Equation 2) used the same independent parameters as Equation 1 and similar relations between these parameters were seen, despite varying absolute values and coefficients. Snowfall accounted for 60% and temperature accounted

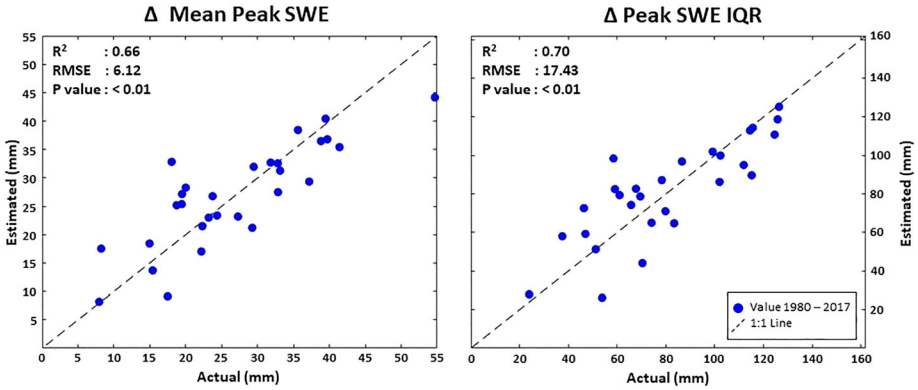

Figure 9. Simulated SnowPALM values (*x* axis) versus estimates (*y* axis) from Equations 1 and 2 that use mean snowfall (log) and mean temperature during the period of snow cover duration as predictors to estimate the interannual variability in mean peak SWE (left) and the interquartile range in peak SWE (right) for the site. The 1:1 line is represented by a dashed line.

for 10% of the data variation for a total of 70% with an RMSE of 17.43 mm and a p value <0.01 (see Figure 9). In both cases, higher snowfall and/or temperature increased the quantity of postfire peak SWE and range of postfire SWE values for the site.

$$\Delta\, mean\ peak\, SWE\,(mm) \ = 0.18^{*}\ \overline{snow}_{SCD} + 1.64\ ^{*}\ \overline{ta}_{SCD} + 0.57 \tag{1}$$

$$\Delta\, peak\, SWE\, IQR\,(mm) \ = 0.36^{*}\ \overline{snow}_{SCD} + 6.24\ ^{*}\ \overline{ta}_{SCD} + 1.48 \tag{2}$$

3.5.2. Melt-Out Date

The postfire mean melt-out date for the field area was up to 5 days later than the prefire values for all years. The range in melt-out date for the field area (Δ melt-out date IQR) increased by up to 55 days for all years (except for two). As with postfire peak SWE, the increased variation in postfire melt-out date included areas within the domain that had both later and earlier postfire melt-out dates (see Figure 5). Estimations of postfire Δ melt-out date displayed much lower correlations to meteorology as postfire Δ peak SWE because melt-out date integrates the effects of both accumulation and ablation.

Interannual variations in Δ melt-out date was best estimated with the (1) cumulative incoming radiation during ablation (Cum. $ISWR_{abl}$) and (2) IQR in temperature during ablation (Ta IQR_{abl}), (Equation 3). This relation resolved 50% of the data variation. Cum. $ISWR_{abl}$ accounted for 43% of variation and temperature accounted for the remaining 7%, with an RMSE of 6.12 mm and a p value <0.01. Δ melt-out date IQR used the same predictors as Equation 3 but demonstrated a reduced fit. Cum. $ISWR_{abl}$, accounted for just over half of the captured variance with an initial R^2 of 0.18. Ta IQR_{abl} increased the R^2 to 0.33 with a RMSE of 14.6 days and a p value <0.01 (Equation 4).

$$\Delta\ \text{mean melt} - \text{out date (days)} = 2.68 \times 10^{-4^{*}}\text{Cum. ISWR}_{\text{abl}} + 0.23^{*}\ \text{Ta IQR}_{\text{abl}} - 2.28 \tag{3}$$

$$\Delta\ \text{melt} - \text{out date IQR (days)} = 1.27 \times 10^{-3^{*}}\text{Cum. ISWR}_{\text{abl}} + 2.20^{*}\ \text{Ta IQR}_{\text{abl}} - 17.6 \tag{4}$$

4. Discussion

4.1. Disturbance Modeling and Model Validation

The increasing likelihood of disturbances occurring in many snow-dominated forested watersheds necessitates improved understanding of the effects of those disturbances on snow resources. In this study, we had the unique opportunity to couple multiple high-resolution (1 m) lidar data sets representing predisturbance and postdisturbance with a snowpack mass and energy budget model includes horizontal canopy influences (SnowPALM model). Although the model has limitations, the ability to integrate three-dimensional canopy information to represent horizontal canopy influences, such as tree shading and longwave radiative effects extending to nearby canopy pixels, is integral for simulating the spatial variability of snowpack in specific

forest canopy classes such as forest edges and gaps (Broxton et al., 2015). This high-resolution model allows for postdisturbance conditions over a large range of prefire and postfire canopy settings to be analyzed (in this case 1.1 million pixels) rather than ground-based measurements or coarser scale model environments that have limited ability to capture the role of prevegetation and postvegetation structure on the spatial distribution of snow.

The model was well validated against two snow pillows with 10 years of data during accumulation, peak SWE and ablation seasons (Figures 3a–3d), a high-resolution lidar-derived SD snapshot that captured peak SWE and midwinter ablation events, and a SD measurement campaign during the ablation period. The lidar validations showed that shading contributed to extremely heterogenous snow distribution patterns, and SnowPALM model pixels that started ablation or experienced midwinter ablation events are also visible in the lidar snapshot (Figures 3e–3f). These were also preserved in the SnowPALM SD estimates where, in a basic example, SD is deeper on the north side of canopy elements and shallower on the south side of canopy elements (Figures 3g and 3h).

4.2. Canopy Parameters

The high-resolution prefire and postfire lidar allowed for a detailed analysis of canopy structure and density. The canopy metrics represent a disturbance from a high-severity fire, where one would expect to see a range of postfire differences that reach complete canopy removal in some areas. However, the canopy density metrics were not able to fully represent this. For example, CC displayed a 12% mean change for the field area (a 26% change for LAI). This contrasts with the structure metrics, aerial imagery analysis, and site visits, all of which showed a much larger change. The canopy structure metrics displayed a range of postfire differences that approached a 100% change relative to the prefire metrics (Table 2).

The inability of the density metrics to represent canopy disturbance is partially due to the large view frame that integrates surrounding canopy elements for the characterization of CC and LAI. However, most snow models (Varhola & Coops, 2013) rely solely on density estimates to describe the forest, which may be problematic when these are used to simulate highly heterogenous canopy conditions or canopy change. Besides higher resolution modeling and improving canopy representation in models, it is important to distinguish between the overhead and surrounding canopy (Mazzotti et al., 2019). For example, two model pixels with the same canopy density may display a completely different spatial arrangement of trees.

4.3. Simulation of Snowpack

Relative to prefire conditions, the means of postfire peak SWE and melt-out date for the site, for all years between 1980 and 2017, were nearly always higher and later, respectively, across a range of interannual climate variability. Despite this, approximately 30% of the domain showed decreases in postfire peak SWE and earlier melt-out date for each water year, which resulted in higher overall variability. This is in general agreement with field observations, where increases and decreases in snow water have been measured at a nearby research site (Harpold, Biederman, et al., 2014), as well as in other environments (Goeking & Tarboton, 2020; Krogh et al., 2020; Maxwell et al., 2019). However, this differs from results of most other modeling studies that have shown only increases in SWE after a forest disturbance (Goeking & Tarboton, 2020). Forest disturbance involves not only the overall removal of the canopy, but changes the forest structure. Therefore, changes in the mass and energy balance are not just dependent upon change in canopy density but how the spatial distribution of trees changes as well. If a model is not of a sufficient resolution to capture fine-scale structure, then the use of just canopy density metrics such as CC and LAI (standard for most snow melt models) at a coarser scale may not appropriately describe the true effect of a forest disturbance. This has been highlighted in other studies as well. Several works including Mazzotti, Essery, Moeser, et al. (2020) and Moeser, Stähli, et al. (2015) showed that the inclusion of canopy structure metrics rather than just canopy density was able to improve snow representation and forested environments. Similarly, Sun et al. (2018) showed improved ablation dynamics from the inclusion of a "mean gap diameter" parameter.

Each water year also had varying postfire increases and decreases in peak SWE and melt-out date. However, the location of the changes were always similar (Figure 5) and could be partially explained by forest structure changes. Similarly, while the magnitude of change differs as the accumulation and ablation seasons progress through time, the locations in the field area that display increases and decreases in SWE change relatively

little. As such, the pattern of canopy disturbance can dictate whether a similar area will experience a generalized increase or decrease in peak SWE and melt-out date.

4.4. RQ1—Correlation of Canopy Structure Classes to Locations of Postfire Changes in Snow

One of the benefits of the high-resolution model was the ability to analyze terrain aspect relative to canopy structure to describe locations of postfire changes in snow distribution and retention. Maxwell et al., 2019 for example, were able to relate areas of postfire increase and decrease to topographic controls, and aspect was a key determinant on location of postfire SWE reductions, where postfire decreases in SWE and earlier melt-out date were measured on south slopes and postfire increases in SWE and later melt-out date were measured on the north slopes. This modeled domain showed a similar but smaller dependence on aspect alone. However, when aspect-based canopy structure was analyzed, we were able to better define locations of postfire peak SWE reductions and earlier melt-out date on forest edges and gaps.

In locations that transitioned to canopy edges after the fire, the largest postfire decreases (up to 55 mm or 77%) were found on south facing edges of a canopy gap $\geq 3H$ in size with a southern terrain aspect (bottom left tile in Figure 6). Canopy gaps displayed similar trends to canopy edges. The largest decreases (up to 117 mm or 57%) were on locations that were initially small canopy edges or gaps that transitioned to larger canopy gaps that increased in size to the south (bottom left tile in Figure 7). Without this direction-based analysis, no significant trends were found with postfire changes in peak SWE and melt-out date on forest edges and gaps. This highlights that the change in gap shape is as important as the change in gap size and the strong control canopy shading can play on subcanopy snow water resources. Canopy shading has been indirectly highlighted in prior work. Snow heterogeneity on forest edges, for example, has been previously linked to aspect (Currier & Lundquist, 2018; Golding & Swanson, 1986; Lawler & Link, 2011; Musselman et al., 2015; Pomeroy et al., 2009; Veatch et al., 2009) and in canopy gaps, differences in snow retention have been linked to the height of the surrounding trees and terrain aspect (Lawler & Link, 2011; Musselman et al., 2015).

In the interior forest, or areas without gaps or edges, the removal of large trees in the local area affected and created larger postfire Δ melt-out date and Δ peak SWE decreases (84 mm or 58%) than removing smaller trees. This represents decreases in interception but increases in downward shortwave radiation from a reduction in canopy shading from the large trees, while maintaining significant longwave radiation from the underlying canopy density. However, in areas where all the canopy was removed from the fire, there were significant increases in peak SWE and later melt-out date, which is in line with many previous studies that showed higher snow quantities in open versus forested areas due to a reduction in interception, canopy sublimation, and longwave radiation (Moeser, Stähli, et al., 2015; Varhola, Coops, Weiler, et al., 2010).

Understanding the link between changes in canopy structure and snow storage is an important step forward in understanding the potential effects of future canopy disturbance events. Specifically, basic relations found between the structural makeup of the interior forest, canopy gaps, and canopy edges and how these change to peak SWE and melt-out date can be used to qualitatively assess the effects of canopy disturbance on snow water resources over larger field domains in this region. These relations can help guide silviculture practices for mitigation of future forest disturbance in this region. For example, minimizing the amount of south facing edges, avoiding the increase of canopy gaps to a southern direction, and thinning smaller trees rather than the larger local trees could all lead toward maximizing SWE and retention time in geographically similar watersheds.

4.5. RQ2—Correlation of Meteorology to Site-Based Changes in Snow

Higher annual snowfall and temperature increased the probability of larger postfire peak SWE for the site and variation of peak SWE within site. However, temperature was not as correlated as snowfall in controlling the amount of peak SWE variation. Unlike postfire changes in peak SWE for the site, changes in melt-out date were less influenced by the mass balance, and more influenced by the energy balance. Increasing sunny skies during ablation (represented from cumulative ISWR during ablation) increased the potential for a later postfire melt-out date for the site and higher melt-out date variation within the site. However, most melt-out date variation could not be explained from this analysis because melt-out date integrates the effects of both accumulation and ablation.

Even though increases in snowfall, temperature, and sunny skies led to a larger range of postfire peak SWE and melt-out date in this field area, similar relations may not be present in other field areas. In this field area, the postdisturbance peak SWE and melt-out date were nonnormally distributed and skewed in the field area, and there were larger areas with increases in peak SWE and later melt-out date than decreases as compared to the predisturbance values. This distribution was partially based on the pattern of canopy disturbance, and any differences in the disturbance pattern would change the SWE distribution and skew (larger areas of SWE loss vs. gain). However, the disturbance pattern and initial structural makeup of the canopy will dictate whether an area will experience a generalized increase or decrease in peak SWE and melt-out date (Harpold et al., 2020; Krogh et al., 2020).

4.6. Transferability of Results to Other Field Sites

The regression equations within this study were used to estimate the utility of using specific canopy metric and meteorological variable pairings to define changes in simulated postfire snow distribution over time. The equations were specific to this field area and may not be transferable to other regions. For example, log transforms were used in the regression equations that represented changes in gap shape and forest edges, or ablation dominant environments. This creates a nonlinear snow distribution pattern and is consistent with nonlinear snow distribution measured on the ground (Figures 1, 3e, and 3f, Currier & Lundquist, 2018; Mazzotti et al., 2019). However, this would not be representative of other areas with a reduced dependence on canopy structure changes. Similarly, the effect of climate variables may differ for other regions. For example, the use of cumulative ISWR during ablation may display diminished predictive utility in areas that have lower canopy shading effects as compared to this field area.

This field area is in a unique high-radiation snow-dominated forested environment at a low latitude (~36°N) and relatively high elevation. This high-radiation environment causes different snow ablation patterns relative to higher latitudes or regions with substantially different weather patterns, and as such, the dependence on forest edges and the size of canopy gaps will most likely diminish in higher latitudes and could explain confounding field observations of postdisturbance snow variability. Seyednasrollah and Kumar (2019) has highlighted the changing relation between long and shortwave radiation on a forested snowpack at varying latitude, climate, canopy density, slope, and aspect. Specifically, Dickerson-Lange et al. (2017) found that at in the U.S. Pacific Northwest at a latitude ranging between ~44°N and 47°N in a comparatively cloudy environment, melt-out date was equivalent under the forest and in the open when these sites started melt season with an equivalent amount of snow. This indicates a reduced dependence on ISWR and canopy shading relative to the Jemez field area. This highlights the interdependence of canopy structure and climate controls to snow heterogeneity and is most likely compounded further by latitude and changing solar zenith angles. The aspect-based canopy structure parameters, which displayed the highest correlations in this study, may display diminished utility in lower radiation environments where canopy density may play a larger role. Further research is needed to decipher how latitude in conjunction with aspect, slope, and prevailing weather conditions will interact with canopy structure in different regions.

4.7. Modeling Challenges, Gaps, and Moving Forward

Harpold, Biederman, et al. (2014) performed an extensive ground-based measurement campaign in a similar field area after the same fire in the Jemez Mountains. There were significant reductions in postfire peak SWE, which were attributed to increasing winter ablation events and a shift toward topographically controlled variability over canopy cover variability. This study does show reductions of postfire peak SWE and midwinter ablation events in line with their study. However, the model displayed fewer areas of postfire SWE decreases relative to the ground-based study that could be attributed to an underestimate of ablation rates. This study did not integrate several other postfire phenomena such as temporary increases in black carbon and burned woody debris falling on the snow surface. All of these have been shown to significantly change the albedo of snow and increase snow melt and sublimation rates over the extent of the burned area (Gleason et al., 2013; Gleason & Nolin, 2016), have persisted for over a decade following a forest fire, and change annually over time (Gleason et al., 2019). More research is needed to better quantify the interplay of fine-scale canopy structure and temporally changing albedo conditions after a disturbance.

Despite the clear advantage of very high-resolution models, challenges still exist in representing physics at these scales. Beer's law was used to model shortwave radiation, which assumes an even canopy

distribution at each grid cell. Therefore, if the grid cell displays canopy, no radiation can enter the subcanopy even if there is a break in the canopy element. Even at this fine scale (1 m), canopy coverage binarization can hamper radiation attenuation estimates using this technique. This highlights the need for the integration of hyperresolution ray-tracing voxel type approaches or lidar based synthetic hemispherical image analysis that can better account for the extreme heterogeneity of canopy and better model shadowing effects in forest gaps (Moeser et al., 2014; Musselman et al., 2013; Webster et al., 2017). Model representations of turbulent heat transfer and longwave radiation suffer similar challenges representing the effects of fine-scale forest structure (Essery et al., 2008; Mahat & Tarboton, 2012; Pomeroy et al., 2009). Webster et al. (2016) highlighted the importance of longwave radiation modeling and displayed that due to the absorption of shortwave radiation by canopy elements, longwave radiation can play a larger role in snow surface net radiation than shortwave radiation (Sicart et al., 2004).

The data availability in this study dictated that the canopy metrics were static in time and only captured changes that occurred ~11 months postfire and did not represent further changes in the canopy layout of the forest to date. More research is needed to quantify potentially spatial variable postfire degradation and regrowth over years following fire occurrence. It is unclear if and how the relations between Δ peak SWE and melt-out date to the generalized structure classes would modulate through time as canopy structure changes with forest recovery. Multiple postfire flyover data sets would be needed to represent canopy structure and density changes from potential forest regrowth after the initial canopy disturbance. An improved representation of changing canopy over time and a postfire snow albedo parameterization could also allow for the temporal evolution of albedo to be integrated in methods similar to those of Gleason and Nolin (2016). Finally, the results only integrate the interaction between canopy and aspect and do not integrate any potential effects of slope angle. It is unclear how slope angle may change the interactions between canopy structure and aspect.

5. Conclusion

Understanding the link between changes in canopy structure and snow storage is an important step forward in understanding the potential effects of future fires and other canopy disturbance events. Specifically, basic relations found between the structural makeup of the interior forest, canopy gaps, and canopy edges and how these change relative to peak SWE and melt-out date can be used to qualitatively assess the effects of canopy disturbance on snow water resources over larger field domains in this region.

This study demonstrated the important influence of canopy structure on snow water resources after a canopy disturbance. Canopy density metrics (CC, LAI), displayed very little skill in representing canopy disturbance and no correlations were found when these were used to estimate postdisturbance change in peak SWE and melt-out date at a high resolution. Our findings indicate that canopy density metrics alone do not properly represent canopy structure variability or canopy change.

The shape of gaps relative to aspect were as important, if not more important, than the size of canopy gaps for representing postdisturbance changes in snow water storage. Similarly, the direction a canopy edge faces relative to surrounding tree height was more important than knowing just how much canopy edges increased. Specifically, if a forest disturbance increases the amount of south facing canopy edges and the canopy gaps become larger in a southern direction, a similar field area may display reductions in peak SWE and earlier melt-out date. The relatively high correlations between changes in these generalized canopy structure classes and locations of post disturbance changes in snow water also highlight the need to better represent these areas in snow models.

These results are especially insightful in snow-dominated forested areas where changes in canopy and climate are the primary drivers of hydrologic shifts (Giles-Hansen et al., 2019; Wei et al., 2013; Zhang et al., 2017). The results are most likely transferable in similar, snow-dominated, low latitude, high-energy forest environments such as those found in the Rio Grande headwaters that have historically had large insect infestations and catastrophic fires, which are projected to increase in the future by 300% to 700% with a 1°C increase in average global temperature in this region (NRC, 2011). Expanding these generalized results into similar regions facing projected forest landscape changes in water sensitive areas could help develop guidelines for resource managers who perform forest thinning and canopy disturbance mitigation measures in order to best optimize water storage.

Data Availability Statement

All lidar data were collected by the National Center for Airborne Laser Mapping (NCALM) and can be downloaded online (at http://www.opentopography.org/). All PRISM adjusted Version 2 of the National Land Data Assimilation System data can be downloaded online (at https://ldas.gsfc.nasa.gov/nldas/v2/forcing). Model data presented in this study are available from Moeser and Shephard (2019); https://doi.org/10.5066/P9BBCSVN). The SnowPALM model is available online (at https://doi.org/10.5281/zenodo.4088788). The vector searching algorithm and the synthetic image creator used to derive canopy metrics from lidar data are available online (at https://doi.org/10.5281/zenodo.4088667).

Acknowledgments

This research was funded by the Department of the Interior South Central Climate Adaptation Science Center, which is managed by the USGS National Climate Change and Wildlife Science Center (EN05ESH). Any use of trade, firm, or product names is for descriptive purposes only and does not imply endorsement by the U.S. Government.

References

Bates, B. C., Kundzewicz, Z. W., Wu, S., & Palutikof, J. P. (Eds) (2008). *Climate change and water. Technical paper of the Intergovernmental Panel on Climate Change* (p. 210). Geneva: IPCC Secretariat.

Bernier, P., & Swanson, R. (1993). The influence of gap size on snow evaporation in the forests of the Alberta foothills. *Canadian Journal of Forest Research*, *23*(2), 239–244.

Biederman, J. A., Somor, A. J., Harpold, A. A., Gutmann, E. D., Breshears, D. D., Troch, P. A., et al. (2015). Recent tree die-off has little effect on streamflow in contrast to expected increases from historical studies. *Water Resources Research*, *51*, 9775–9789. https://doi.org/10.1002/2015WR017401

Booker, J. F., Michelsen, A. M., & Ward, F. A. (2005). Economic impact of alternative policy responses to prolonged and severe drought in the Rio Grande Basin. *Water Resources Research*, *41*, W02026. https://doi.org/10.1029/2004WR003486

Broxton, P. D., Harpold, A. A., Biederman, J. A., Troch, P. A., Molotch, N. P., & Brooks, P. D. (2015). Quantifying the effects of vegetation structure on snow accumulation and ablation in mixed-conifer forests. *Ecohydrology*, *8*(6), 1073–1094. https://doi.org/10.1002/eco.1565

Buma, B., & Livneh, B. (2017). Key landscape and biotic indicators of watersheds sensitivity to forest disturbance identified using remote sensing and historical hydrography data. *Environmental Research Letters*, *12*(7), 074028. https://doi.org/10.1088/1748-9326/aa7091

Church, J. (1933). Snow surveying: Its principles and possibilities. *Geographical Review*, *23*(4), 529–563.

Currier, W. R., & Lundquist, J. D. (2018). Snow depth variability at the forest edge in multiple climates in the western United States. *Water Resources Research*, *54*, 8756–8773. https://doi.org/10.1029/2018WR022553

deBuys, W. (2001). Navigating the river of our future: The Rio Poco-Grande. *Natural Resources Journal*, *41*(2), 265–281. Retrieved from. http://www.jstor.org/stable/24888574

Deems, J. S., Painter, T. H., & Finnegan, D. C. (2013). Lidar measurement of snow depth: A review. *Journal of Glaciology*, *59*(215), 467–479. https://doi.org/10.3189/2013JoG12J154

Desilets, D. (2009). Monitoring land-surface water with cosmic-ray neutrons. Retrieved from http://www.osti.gov/scitech/servlets/purl/1142096. Accessed 15 Aug.2016

Dickerson-Lange, S., Gersonde, R., Hubbart, J., Link, T., Nolin, A., Perry, G., et al. (2017). Snow disappearance timing is dominated by forest effects on snow accumulation in warm winter climates of the Pacific Northwest, United States. *Hydrological Processes*, *31*(10), 1846–1862. https://doi.org/10.1002/hyp.11144

Essery, R., Morin, S., Lejeune, Y., & Ménard, B. C. (2013). A comparison of 1701 snow models using observations from an alpine site. *Advances in Water Resources*, *55*, 131–148. https://doi.org/10.1016/j.advwatres.2012.07.013

Essery, R., & Pomeroy, J. (2001). Soil-vegetation-atmosphere transfer schemes and large-scale hydrological models international association of hydrological science conference, Maastricht, Netherlands, (pp. 343–347).

Essery, R., Pomeroy, J., Ellis, C., & Link, T. (2008). Modelling longwave radiation to snow beneath forest canopies using hemispherical photography or linear regression. *Hydrological Processes*, *22*(15), 2788–2800.

Essery, R., Rutter, N., Pomeroy, J., Baxter, R., Stähli, M., Gustafsson, D., et al. (2009). SNOWMIP2 an evaluation of forest snow process simulations. *Bulletin of the American Meteorological Society*, *90*(8), 1120–1135. https://doi.org/10.1175/2009BAMS2629.1

Furniss, M., Staab, B., Hazelhurst, S., Clifton, C., Roby, K., Ilhadrt, B., & Edwards, P. (2010). Water, climate change, and forests: Watershed stewardship for a changing climate. General Technical Report PNW-GTR812, (June), 75. https://doi.org/10.1017/CBO9781107415324.004

Giles-Hansen, K., Li, Q., & Wei, X. (2019). The cumulative effects of forest disturbance and climate variability on streamflow in the Deadman River watershed. *Forests*, *10*(2), 9–11. https://doi.org/10.3390/f10020196

Gleason, K. E., McConnell, J. R., Arienzo, M. M., Chellman, N., & Calvin, W. M. (2019). Four-fold increase in solar forcing on snow in western U.S. burned forests since 1999. *Nature Communications*, *10*(1), 1–8. https://doi.org/10.1038/s41467-019-09935-y

Gleason, K. E., & Nolin, A. W. (2016). Charred forests accelerate snow albedo decay: Parameterizing the post-fire radiative forcing on snow for three years following fire. *Hydrological Processes*, *30*, 3855–3870. https://doi.org/10.1002/hyp.10897

Gleason, K. E., Nolin, A. W., & Roth, T. R. (2013). Charred forests increase snowmelt: Effects of burned woody debris and incoming solar radiation on snow ablation. *Geophysical Research Letters*, *40*, 4654–4661. https://doi.org/10.1002/grl.50896

Goeking, S. A., & Tarboton, D. G. (2020). Forests and water yield: A synthesis of disturbance effects on streamflow and snowpack in western coniferous forests. *Journal of Forestry*, *118*(2), 172–192. https://doi.org/10.1093/jofore/fvz069

Golding, D. L., & Swanson, R. H. (1986). Snow distribution in clearings and adjacent forest. *Water Resources Research*, *22*(13), 1931–1940.

Harder, P., Pomeroy, J., & Helgason, W. (2019). Advances in mapping sub-canopy snow depth with unmanned aerial vehicles using structure from motion and lidar techniques. *The Cryosphere Discussions*. https://www.the-cryosphere-discuss.net/tc-2019-284/tc-2019-284.pdf

Harpold, A. A., Biederman, J. A., Condon, K., Merino, M., Korgaonkar, Y., Nan, T., & Brooks, P. D. (2014). Changes in snow accumulation and ablation following the Las Conchas forest fire, New Mexico, USA. *Ecohydrology*, *7*(2), 440–452. https://doi.org/10.1002/eco.1363

Harpold, A. A., Guo, Q., Molotch, N., Brooks, P. D., Bales, R., Fernandez-Diaz, J. C., & Lucas, R. (2014). Lidar-derived snowpack data sets from mixed conifer forests across the western United States. *Water Resources Research*, *50*, 2749–2755. https://doi.org/10.1002/2013WR013935

Harpold, A. A., Krogh, S., Kohler, M., Eckberg, D., Greenberg, J., Sterle, G., & Broxton, P. D. (2020). Increasing the efficacy of forest thinning for snow using high-resolution modeling: A proof of concept in the Lake Tahoe Basin, California, USA. *Ecohydrology*. https://doi.org/10.1002/eco.2203

Harpold, A. A., Marshall, J. A., Lyon, S. W., Barnhart, T. B., Fisher, B. A., Donovan, M., et al. (2015). Laser vision: Lidar as a transformative tool to advance critical zone science. *Hydrology and Earth System Sciences*, *19*(6), 2881–2897. https://doi.org/10.5194/hess-19-2881-2015

Hedstrom, N. R., & Pomeroy, J. (1998). Measurements and modeling of snow interception in the boreal forest. *Hydrological Processes*, *12*(10), 1611–1625. https://doi.org/10.1002/(SICI)1099-1085(199808/09)12:10/11<1611::AID-HYP684>3.0.CO;2-4

Kostadinov, T., Schumer, R., Hausner, M., Borman, K., Gaffney, R., McGwire, K., et al. (2019). Watershed-scale mapping of fractional snow cover under confer forest canopy using lidar. *Remote Sensing of Environment*, *222*, 34–49. https://doi.org/10.1016/j.rse.2018.11.037

Krogh, S. A., Broxton, P. D., Manley, P. N., & Harpold, A. A. (2020). Using process-based snow modeling and lidar to predict the effects of forest thinning on the northern Sierra Nevada snowpack. *Frontiers in Forests and Global Change*. https://doi.org/10.3389/ffgc.2020.00021

Lawler, R. R., & Link, T. E. (2011). Quantification of incoming all-wave radiation in discontinuous forest canopies with application to snowmelt prediction. *Hydrological Processes*, *25*(21), 3322–3331. https://doi.org/10.1002/hyp.8150

Liston, G. E., & Elder, K. (2006). A distributed snow-evolution modeling system (SnowModel). *Journal of Hydrometeorology*, *7*(6), 1259–1276. https://doi.org/10.1175/JHM548.1

Lundberg, A., & Halldin, S. (2001). Snow interception evaporation—Rates, processes and measurement techniques. *Theoretical and Applied Climatology*, *70*, 117–133.

Mahat, V., & Tarboton, D. G. (2012). Canopy radiation transmission for an energy balance snowmelt model. *Water Resources Research*, *48*, W01534. https://doi.org/10.1029/2011WR010438

Maxwell, J., & St Clair, S. B. (2019). Snowpack properties vary in response to burn severity gradients in montane forests. *Environmental Research Letters*, *14*, 124094. https://doi.org/10.1088/1748-9326/ab5de8

Maxwell, J. D., Call, A., & St Clair, S. B. (2019). Wildfire and topography impacts on snow accumulation and retention in montane forests. *Forest Ecology and Management*, *432*, 256–263.

Mazzotti, G., Currier, W., Deems, J., Pflug, J., Lundquist, J., & Jonas, T. (2019). Revisiting snow cover variability and canopy structure within forest stands: Insights from airborne lidar data. *Water Resources Research*, *55*, 6198–6216. https://doi.org/10.1029/2019WR024898

Mazzotti, G., Essery, R., Moeser, D., & Jonas, T. (2020). Resolving small-scale forest snow patterns with an energy balance snow model and a 1-layer canopy. *Water Resources Research*, *56*, e2019WR026129. https://doi.org/10.1029/2019WR026129

Mazzotti, G., Essery, R., Webster, C., Malle, J., & Jonas, T. (2020). Process-level evaluation of a hyper-resolution forest snow model using distributed multisensor observations. *Water Resources Research*, *56*, e2020WR027572. https://doi.org/10.1029/2020WR027572

Moeser, C.D., & Shephard, Z.M. (2019). Data release: The effects of wildfire on snow water resources estimated from canopy disturbance patterns and meteorological conditions. U.S. Geological Survey data release. https://doi.org/10.5066/P9BBCSVN

Moeser, D., Mazzotti, G., Helbig, N., & Jonas, T. (2016). Representing spatial variability of forest snow: Implementation of a new interception model. *Water Resources Research*, *52*, 1208–1226. http://doi.org/10.1002/2015WR017961

Moeser, D., Morsdorf, F., & Jonas, T. (2015). Novel forest structure metrics from airborne lidar data for improved snow interception estimation. *Agricultural and Forest Meteorology*, *208*, 40–49. https://doi.org/10.1016/j.agrformet.2015.04.013

Moeser, D., Roubinek, J., Schleppi, P., Morsdorf, F., & Jonas, T. (2014). Canopy closure, LAI and radiation transfer from airborne lidar synthetic images. *Agricultural and Forest Meteorology*, *197*, 158–168. https://doi.org/10.1016/j.agrformet.2014.06.008

Moeser, D., Stähli, M., & Jonas, T. (2015). Improved snow interception modeling using canopy parameters derived from airborne LIDAR data. *Water Resources Research*, *51*, 5041–5051. https://doi.org/10.1002/2014WR016724

Montesi, J., Elder, K., Schmidt, R. A., & Davis, R. E. (2003). Sublimation of intercepted snow within a subalpine forest canopy at two elevations. *Journal of Hydrometeorology*, *5*(5), 763–773.

Muldavin, E. & Tonne, P. (2003). A vegetation survey and preliminary ecological assessment of Valles Caldera National Preserve, New Mexico Natural Heritage New Mexico final report to Valles Caldera National Preserve, New Mexico. 73p + App.

Musselman, K. N., Margulis, S. A., & Molotch, N. P. (2013). Estimation of solar direct beam transmittance of conifer canopies from airborne lidar. *Remote Sensing of Environment*, *136*, 402–415. https://doi.org/10.1016/j.rse.2013.05.02

Musselman, K. N., Pomeroy, J. W., & Link, T. E. (2015). Variability in shortwave irradiance caused by forest gaps: Measurements, modelling, and implications for snow energetics. *Agricultural and Forest Meteorology*, *207*, 69–82. https://doi.org/10.1016/j.agrformet.2015.03.014

National Park Service (2019). Valles Caldera National Preserve New Mexico. Website. Last accessed 27 august 2019. https://www.nps.gov/vall/index.htm

National Research Council (NRC) (2011). *Climate stabilization targets: Emissions, concentrations, and impacts over decades to millennia. National Research Council*. Washington, DC, USA: The National Academies Press.

Pomeroy, J., Gray, D. M., Shook, K., Toth, B., Essery, R., Pietroniro, A., & Hedstrom, N. (1998). An evaluation of snow accumulation and ablation processes for land surface modeling. *Hydrological Processes*, *12*, 2339–2367.

Pomeroy, J. W., Marks, D., Link, T., Ellis, C., Hardy, J., Rowlands, A., & Granger, R. (2009). The impact of coniferous forest temperature on incoming longwave radiation to melting snow. *Hydrological Processes*, *23*, 2513–2525. https://doi.org/10.1002/hyp.7325

Schleppi, P., Conedera, M., Sedivy, I., & Thimonier, A. (2007). Correcting non-linearity and slope effects in the estimation of the leaf area index of forests from hemispherical photographs. *Agricultural and Forest Meteorology*, *144*, 236–242. https://doi.org/10.1016/j.agrformet.2007.02.004

Sexstone, G. A., Clow, D., Fassnacht, S., Liston, G., Hiemstra, C., Knowles, J., & Penn, C. (2018). Snow sublimation in mountain environments and its sensitivity to forest disturbance and climate warming. *Water Resources Research*, *54*, 1191–1211. https://doi.org/10.1002/2017WR021172

Seyednasrollah, B., & Kumar, M. (2019). How surface radiation on forested snowpack changes across a latitudinal gradient. *Hydrology*, *6*(3), 62. https://doi.org/10.3390/hydrology6030062

Sicart, J. E., Essery, R. L. H., Pomeroy, J. W., Hardy, J., Link, T., & Marks, D. (2004). A sensitivity study of daytime net radiation during snowmelt to forest canopy and atmospheric conditions. *Journal of Hydrometeorology*, *5*(5), 774–784. https://doi.org/10.1175/1525-7541(2004)005<0774:ASSODN>2.0.CO;2

Skartveit, A., & Olseth, J. A. (1987). A model for the diffuse fraction of hourly global radiation. *Solar Energy*, *38*(4), 271–274. https://doi.org/10.1016/0038-092X(87)90049-1

Stegman, S. V. (1996). Snowpack changes resulting from timber harvest: Interception, redistribution, and evaporation. *Journal of the American Water Resources Association*, *32*(6), 1353–1360. https://doi.org/10.1111/j.1752-1688.1996.tb03503.x

Stevens, J. T. (2017). Scale-dependent effects of post-fire canopy cover on snowpack depth in montane coniferous forests. *Ecological Applications*, *27*(6), 1888–1900. https://doi.org/10.1002/eap.1575

Sun, N., Wigmosta, M., Zhou, T., Lundquist, J., Dickerson-Lange, S., & Cristea, N. (2018). Evaluating the functionality and streamflow impacts of explicitly modelling forest–snow interactions and canopy gaps in a distributed hydrologic model. *Hydrological Processes*, *32*(13), 2128–2140. https://doi.org/10.1002/hyp.13150

Suzuki, K.N., Yuichiro, O., & Takeshi, N. (2003). Effect of snow interception on the energy balance above deciduous and coniferous forests during a snowy winter. Paper presented at the IUGG-Water Resource Systems, Sapporo, Japan 2003.

U.S. Forest Service (2018). *CP district-wide salvage project final environmental impact statement Conejos and Rio Grande Counties*. La Jara, Colorado: Colorado. Rio Grande National Forest. https://www.fs.usda.gov/nfs/11558/www/nepa/103623_FSPLT3_4292373.pdf

U.S. Forest Service. (2019). Rio Grande National Forest. Website. https://www.fs.usda.gov/riogrande

Varhola, A., Coops, N., Bater, C., Teti, P., Boon, S., & Weiler, W. (2010). The influence of ground- and lidar-derived forest structure metrics on snow accumulation and ablation in disturbed forests. *Canadian Journal of Forest Research*, *40*(4), 812–821.

Varhola, A., & Coops, N. C. (2013). Estimation of watershed-level distributed forest structure metrics relevant to hydrologic modeling using lidar and Landsat. *Journal of Hydrology*, *487*, 70–86. https://doi.org/10.1016/j.jhydrol.2013.02.032

Varhola, A., Coops, N. C., Weiler, M., & Moore, R. D. (2010). Forest canopy effects on snow accumulation and ablation: An integrative review of empirical results. *Journal of Hydrology*, *392*(3–4), 219–233. https://doi.org/10.1016/j.jhydrol.2010.08.009

Veatch, W., Brooks, P. D., Gustafson, J. R., & Molotch, N. (2009). Quantifying the effects of forest canopy cover on net snow accumulation at a continental, mid-latitude site. *Ecohydrology*, *2*(2), 115–128.

Webster, C., Rutter, N., & Jonas, T. (2017). Improving representation of canopy temperatures for modeling subcanopy incoming longwave radiation to the snow surface. *Journal of Geophysical Research: Atmospheres*, *122*, 9154–9172. https://doi.org/10.1002/2017JD026581

Webster, C., Rutter, N., Zahner, F., & Jonas, T. (2016). Modeling subcanopy incoming longwave radiation to seasonal snow using air and tree trunk temperatures. *Journal of Geophysical Research: Atmospheres*, *121*, 1220–1235. https://doi.org/10.1002/2015JD024099

Wei, X., Liu, W., & Zhou, P. (2013). Quantifying the relative contributions of forest change and climatic variability to hydrology in large watersheds: A critical review of research methods. *Water (Switzerland)*, *5*(2), 728–746. https://doi.org/10.3390/w5020728

Winstral, A., & Marks, D. (2002). Simulating wind fields and snow redistribution using terrain-based parameters to model snow accumulation and melt over a semi-arid mountain catchment. *Hydrological Processes*, *16*(18), 3585–3603. https://doi.org/10.1002/hyp.1238

Zellweger, F., Baltensweiler, A., Schleppi, P., Huber, M., Küchler, M., Ginzler, C., & Jonas, T. (2019). Estimating below-canopy light regimes using airborne laser scanning: An application to plant community analysis. *Ecology and Evolution*, *9*(16), 9149–9159. https://doi.org/10.1002/ece3.5462

Zhang, M., Liu, N., Harper, R., Li, Q., Liu, K., Wei, X., et al. (2017). A global review on hydrological responses to forest change across multiple spatial scales: Importance of scale, climate, forest type and hydrological regime. *Journal of Hydrology*, *546*, 44–59. https://doi.org/10.1016/j.jhydrol.2016.12.040